

# Identification of a PFAS hyperaccumulator and elucidation of its translocation mechanism for sustainable phytoremediation

Received: 2 April 2025

Accepted: 9 October 2025

Published online: 21 November 2025

 Check for updates

Xinyu Guo<sup>1,2</sup>, Xinxin Zhang<sup>1</sup>, Jie Chen<sup>1,2</sup>, Wenyu Shan<sup>1</sup>, Runyun Wang<sup>1</sup>, Ke Wang<sup>1</sup>, Zhenhuan Chen<sup>1</sup>, Lei Wang<sup>1,2,3</sup>✉ & Yanyan Zhang<sup>1,2,3</sup>✉

Remediation of soils contaminated by the globally concerning per- and polyfluoroalkyl substances (PFAS) is imperative yet challenging. Herein, we identify a PFAS hyperaccumulator, the herbaceous *Oenothera rosea*, in soil near a fluorochemical facility and demonstrate root-to-shoot translocation factors of 3.07 – 58.6 for 18 distinct PFAS. Comparative hydroponic/pot experiments using conspecifics from non-polluted areas confirm that hyperaccumulation arises from domestication after prolonged PFAS exposure. Root cell wall pectin and hemicellulose are critical PFAS binding sites, significantly affecting root-to-shoot translocation. Subcellular and transcriptomic analyses reveal that the hyperaccumulating *O. rosea* undergoes minimal cell wall remodeling under PFAS stress, a signature of adaptive evolution. Life cycle assessment further validates the environmental superiority of an integrated strategy combining *O. rosea* phytoremediation with biomass pyrolysis for PFAS destruction and biochar production, achieving a net-negative carbon footprint (–17.9 kg CO<sub>2</sub>/ton soil). Our work provides a comprehensive framework for PFAS remediation, from hyperaccumulator identification to sustainable field application.

Per- and polyfluoroalkyl substances (PFAS) are globally concerning pollutants but also indispensable industrial chemicals because of their superior surface activity and chemical stability<sup>1–3</sup>. Their persistence and toxicity have led to worldwide restrictions on long-chain legacy PFAS, including perfluorooctanesulfonic acid (PFOS), perfluorooctanoic acid (PFOA), and perfluorohexanesulfonic acid (PFHxS), under the Stockholm Convention<sup>4</sup>. However, to meet market demand for these functionally essential chemicals, numerous novel PFAS structures have been developed, resulting in their continuous release into the environment<sup>5–8</sup>. Consequently, extraordinarily high levels of diverse PFAS (e.g., PFOA reaching 2241 ng/g) were frequently

observed in soils near fluorochemical facilities, representing one of the most significant PFAS sources<sup>9,10</sup>. These soil-borne PFAS pose severe long-term risk to both ecosystem integrity and public health through plant uptake and trophic transfer<sup>11,12</sup>, imposing urgent need to develop effective, sustainable remediation technologies.

Despite intensive efforts, removing PFAS from soil remains challenging. Microbial degradation can barely break the strong C–F bonds in PFAS<sup>13</sup>. Physicochemical destruction and conventional phase-transfer technologies (e.g., immobilization or soil washing) are constrained by high costs, limited treatment efficiency, poor scalability, and potential damage to soil functionality<sup>14–18</sup>. In contrast,

<sup>1</sup>Key Laboratory of Coastal Environment and Resources of Zhejiang Province, School of Engineering, Westlake University, Hangzhou, Zhejiang, China.

<sup>2</sup>Institute of Advanced Technology, Westlake Institute for Advanced Study, Hangzhou, Zhejiang, China. <sup>3</sup>Research Center for Industries of the Future, Westlake University, Hangzhou, Zhejiang, China. ✉e-mail: [wang\\_lei@westlake.edu.cn](mailto:wang_lei@westlake.edu.cn); [zhangyanyan@westlake.edu.cn](mailto:zhangyanyan@westlake.edu.cn)

phytoremediation represents an environmentally sustainable solution for continuous PFAS removal without soil disturbance or secondary pollution<sup>19,20</sup>. The economic feasibility of this approach is further enhanced through valorization of harvested biomass, including bio-fuel conversion and lignin/cellulose extraction<sup>21,22</sup>. However, practical application of this technology has been hindered by the lack of PFAS hyperaccumulators meeting established criteria (leaf concentration factor, LCF > 10; translocation factor, TF > 3)<sup>23,24</sup>. Existing studies report LCF and TF values in terrestrial plants far below these thresholds<sup>25–29</sup>, indicating that PFAS hyperaccumulation is not inherent but requires adaptive evolution through chronic exposure<sup>30</sup>—a pattern mirroring historical discovery of metal hyperaccumulators<sup>23,24</sup>. Unfortunately, prior studies have overlooked that PFAS hyperaccumulators likely thrive only in soils with sustained PFAS emissions, particularly near fluorochemical facilities. Thus, target screening in contaminated areas and mechanistic studies on PFAS translocation are critical to advance effective phytoremediation strategies.

The root cell wall has been identified as the dominant binding site for PFAS<sup>6</sup>, but more specific subcellular components involved and their modification under PFAS exposure remain unexplored. Comparative analyses between PFAS hyperaccumulators and non-hyperaccumulating conspecifics at tissue, cellular, and molecular levels are needed to identify key determinants of root uptake and root-to-shoot translocation. Transcriptomic analyses (RNA-seq) could further unravel functional genes and expression profiles underlying PFAS hyperaccumulation, as demonstrated for other contaminants<sup>31–33</sup>. On the other hand, sustainability of remediation technologies must be evaluated through life cycle assessment (LCA), particularly accounting for global warming potential, fossil resource scarcity, and ecotoxicity. PFAS-loaded biomass after phytoremediation requires proper management to avoid secondary pollution. Converting harvested biomass into high-value products such as biochar could enhance circular sustainability<sup>21,34</sup>. However, the efficacy and long-term safety of such post-treatment methods for PFAS elimination remain unverified.

Herein, we identify *Oenothera rosea* as a PFAS hyperaccumulator in soils near a fluorochemical facility and elucidate its hyperaccumulation mechanisms (Fig. 1a). To our knowledge, this represents the first documented PFAS hyperaccumulator with TF greater than 3 for 18 distinct PFAS. We perform controlled hydroponic/pot experiments to validate this domestication-driven hyperaccumulating capacity compared to the uncontaminated conspecific. We then conduct subcellular fractionation to reveal key binding components, with further RNA-seq analyses to reveal the genetic basis of hyperaccumulation. Additionally, we perform scenario and LCA analyses to demonstrate the superior effectiveness and sustainability of phytoremediation combined with biomass pyrolysis compared to conventional physical and chemical technologies. Our findings provide both a practical guide for hyperaccumulator screening and a closed-loop solution for PFAS contaminated soils, advancing fundamental science and environmental remediation technology.

## Results and discussion

### Screening PFAS hyperaccumulators in soil near a fluorochemical facility

Scaling PFAS phytoremediation requires identifying adapted hyperaccumulators<sup>35</sup>. Unlike previous random screening approaches<sup>20,36</sup>, we strategically sampled eight woody/herbaceous species within 2 km downstream of a fluorochemical facility to target evolutionarily selected PFAS accumulation traits (Supplementary Fig. 1). The soil sites have undergone moderate PFAS exposure for over 60 years. Eighty-two PFAS in soil and plant tissues were quantified (details in Supplementary Figs. 2–5 and Tables 1–6) to calculate concentrations factors in roots (RCF), stems (SCF) and leaves (LCF), along with TF values (Eqs. 1–4). Stems and leaves were washed by methanol/H<sub>2</sub>O (1:1, v/v) to remove

surface adsorbed PFAS originating from atmospheric deposition (Supplementary Fig. 6). *O. rosea* outperformed other species, showing (i) the highest aboveground uptake capacity, (ii) high SCF and LCF values, and (iii) notably high TF values (Figs. 1, 2). The consistent achievement of LCF > 10 and TF > 3 for 18 distinct PFAS establishes *O. rosea* as the first documented PFAS hyperaccumulator, to our knowledge.

The total concentration of 82 target PFAS ( $\sum_{82}$ PFAS) in surface soils (0–15 cm) was 21.1–32.4 ng/g (Supplementary Fig. 7 and Table 7), with 42 PFAS being detected. The concentration level is comparable to those reported near fluorochemical industries (reviewed in Supplementary Table 8) and is over 20 times of those in background soils sampled herein (0.72–1.04 ng/g) or reported elsewhere (0.05–1.12 ng/g)<sup>37,38</sup>. PFOA and HFPO-TrA collectively accounted for >72% of  $\sum_{82}$ PFAS, consistent with their use as processing acids during fluoropolymer production<sup>10</sup>. The moderate soil PFAS levels warrant the suitability of the sampling sites for screening PFAS hyperaccumulators.

$\sum_{82}$ PFAS in the sampled plants were significantly higher than those from background sites (Fig. 1b). Most PFAS were retained in leaves (203.1–1102.5 ng/g), followed by stems (24.2–170.6 ng/g) and roots (56.0–100.9 ng/g), with minimal accumulation in the bark of woody plants (16.7–36.7 ng/g). PFPrA was the dominant species in the leaf and stem, accounting for 24.5–80.4% of  $\sum_{82}$ PFAS, whereas PFOA (24.1–63.3%) and HFPO-TrA (8.70–39.2%) were the major compounds in the root and bark (Fig. 1c). *O. rosea* stood out for its highest uptake capacity in the aboveground parts, with  $\sum_{82}$ PFAS of 1102.5 ng/g in leaves and 170.6 ng/g in stems, significantly exceeding those of other plants (203.1–602.4 ng/g and 24.2–100.5 ng/g) (Fig. 1b).

To compare PFAS accumulation capacity across the sampled plants, we calculated RCF, SCF, and LCF values for  $\sum_{82}$ PFAS and 27 individual PFAS with substantial soil concentrations. *O. rosea* exhibited significantly higher SCF (6.27) and LCF (40.5) for  $\sum_{82}$ PFAS than other species (1.10–3.57 and 6.28–21.1,  $p < 0.05$ ), despite comparable RCF values (3.09 vs. 2.52–3.12) (Fig. 2a). *O. rosea* also showed the highest SCF and LCF for most individual PFAS, with 10 SCF and 19 LCF values exceeding the hyperaccumulation threshold (10). Although *Solidago canadensis*, *Erigeron annuus*, and the four wood plants had LCF values surpassing 10 for certain PFAS, *O. rosea* distinguished itself as the most effective hyperaccumulator owing to the larger magnitude of LCF and the broader range of PFAS accumulated.

The TF of individual PFAS (Eq. 4) is a more critical parameter for assessing hyperaccumulation potential, as only those transported to shoots can be harvested for continuous phytoextraction<sup>21,39</sup>. Herbaceous species (excluding *Acorus calamus*) showed significantly higher TF values for  $\sum_{82}$ PFAS (4.57–9.20) than woody plants (2.64–3.34), with *O. rosea* exhibiting the highest TF (9.20) (Fig. 2a). This suggests that herbaceous species have stronger pollution adaptation capabilities, which may be attributed to their shorter generational cycles facilitating faster evolutionary response to the decade-long PFAS exposure. Notably, *O. rosea* demonstrated TF values > 3 for 18 PFAS, with the highest value observed for PFPrA (58.6), followed by PFBA (14.1),  $\omega$ H-PFBA (11.6), and HFPO-DA (11.6). The dominant PFOA and HFPO-TrA had TF values of 4.67 and 5.76, respectively.

The superior translocation ability of *O. rosea* for PFAS was further validated by culturing the field-sampled *O. rosea*, *A. calamus*, *S. canadensis* and *E. annuus* in a nutrient solution containing 200  $\mu$ g/mL PFOA. SEM-EDS imaging revealed strong and comparable fluorine signals in the root cross-sections of all species but significantly stronger signals in the stems of *O. rosea* compared to others (Fig. 2b; Supplementary Fig. 8). These observations align with the comparable RCF values for PFOA among the four species (3.27–3.73) but much higher TF values in *O. rosea* (4.67) than the others (0.43–1.78). The results reinforce that only *O. rosea* is uniquely capable of efficiently transporting PFAS from root to shoot.

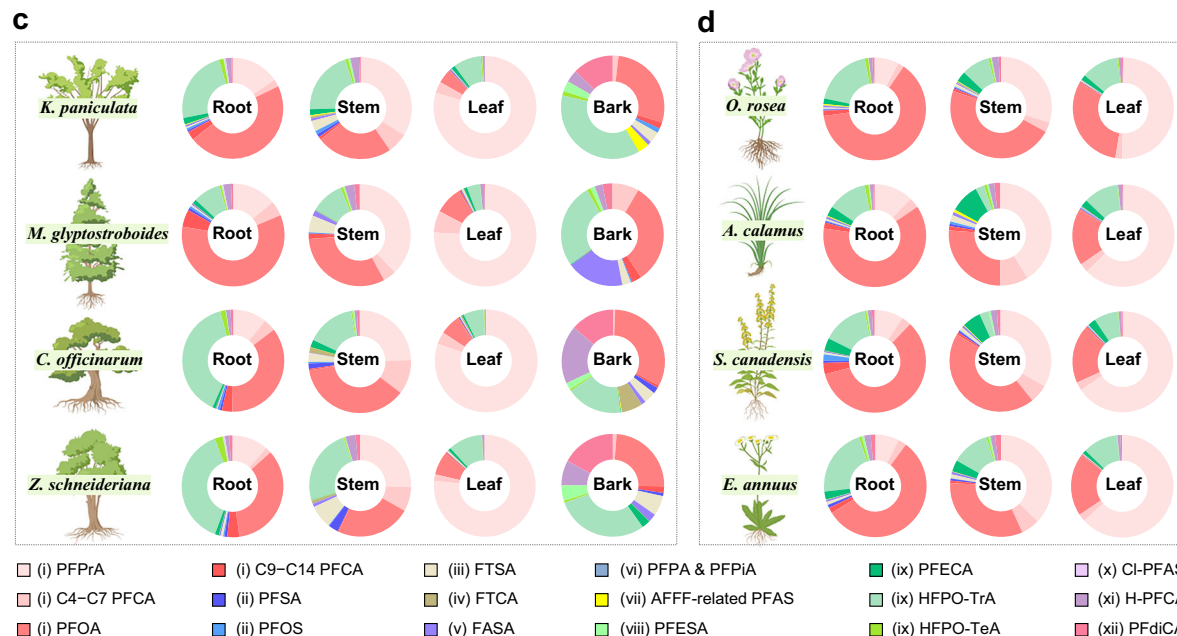
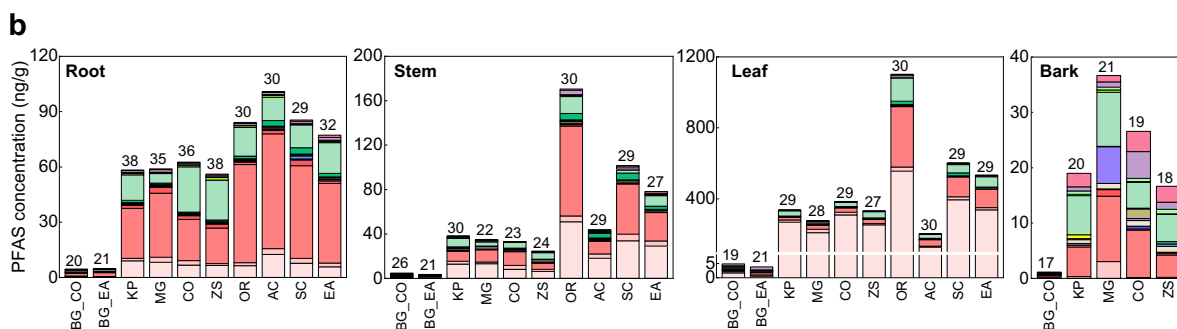
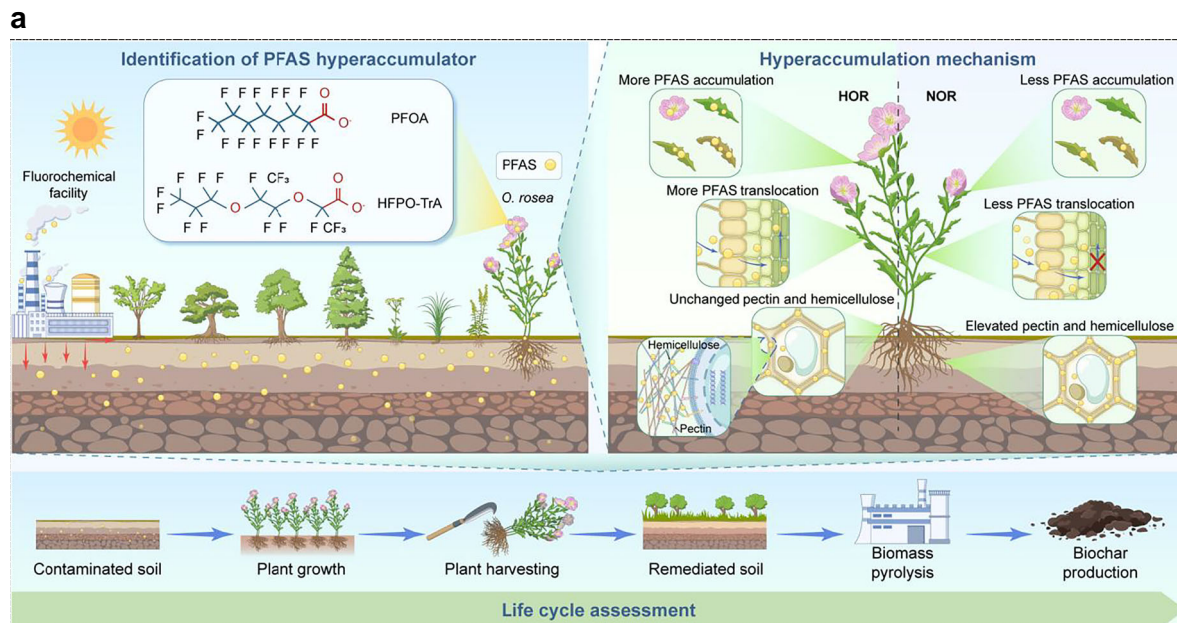


**Fig. 1 | Screening of PFAS hyperaccumulating plants near a fluorochemical facility.** **a** Conceptual schematic of identification of PFAS hyperaccumulator, hyperaccumulation mechanism, and life cycle assessment (LCA) of phytoremediation in PFAS-contaminated soil (details in the text). NOR: non-hyperaccumulating *O. rosea* population; HOR: hyperaccumulating *O. rosea* population. **b** Concentrations of 18 PFAS classes in the root, stem, leaf and bark of the sampled plants near a fluorochemical facility (KP *K. paniculata*, MG *M.*

*glyptostroboides*, CO *C. officinarum*, ZS *Z. schneideriana*, OR *O. rosea*, AC *A. calamus*, SC *S. canadensis*, EA *E. annuus*, BG\_CO and BG\_EA refer to plants sampled from background areas). The numbers above bar charts represent the types of PFAS detected. **c** Relative abundance of individual PFAS and PFAS classes in different parts of four woody plants. **d** Relative abundance of individual PFAS and PFAS classes in different parts of four herbaceous plants. Source data are provided as a Source Data file.

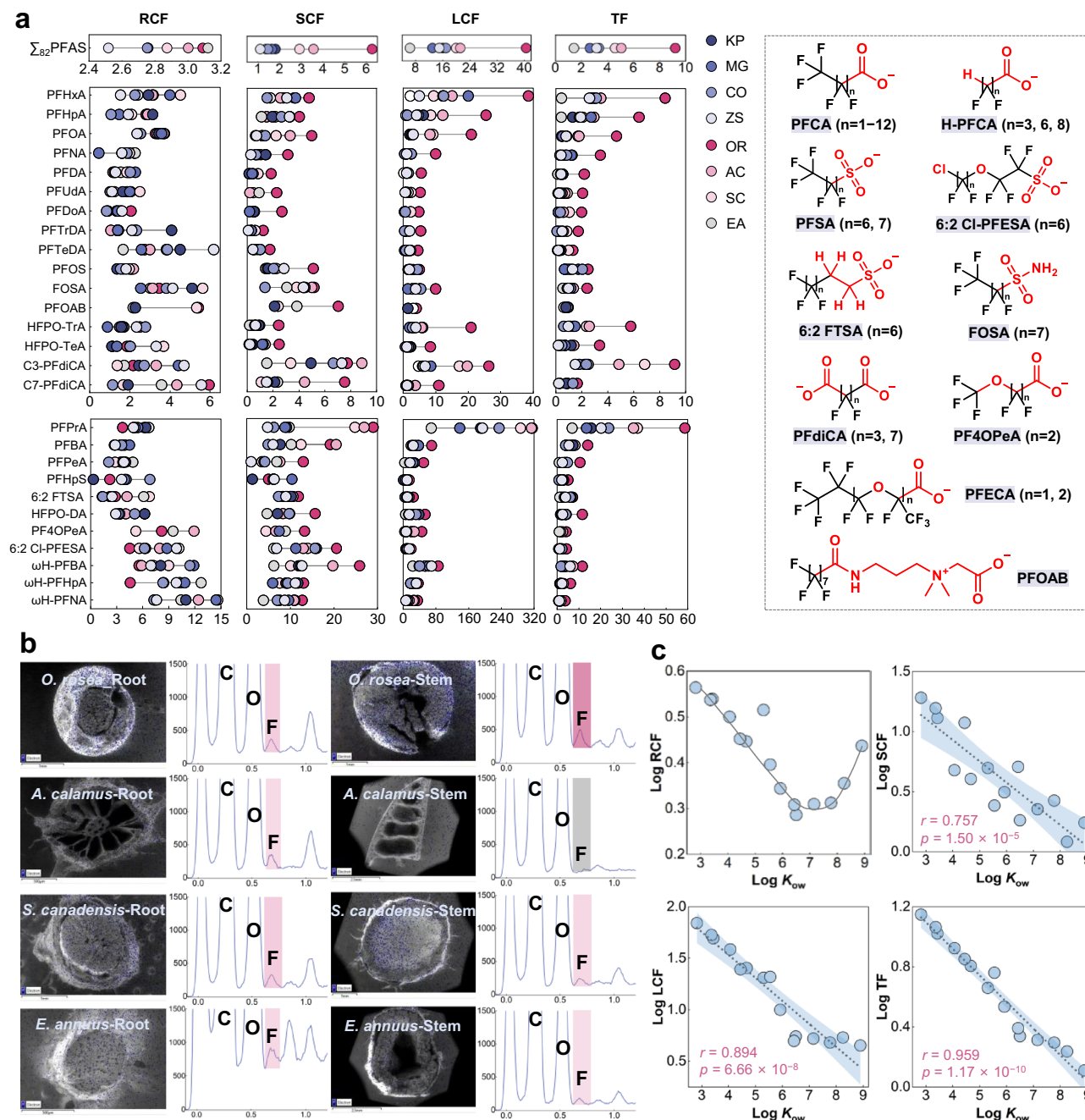


**Fig. 2 | Assessment of bioaccumulation factors of PFAS in plants.**

**a** Concentration factors in the root (RCF), stem (SCF), and leaf (LCF), and the translocation factors (TF) of the sampled plants for  $\Sigma_{82}$ PFAS and 27 individual PFAS with substantial concentrations in the soil. The structures of PFAS are provided. KP, MG, CO, ZS, OR, AC, SC, EA, refer to *K. paniculate*, *M. glyptostroboides*, *C. officinarum*, *Z. schneideriana*, *O. rosea*, *A. calamus*, *S. canadensis*, and *E. annuus*, respectively. **b** SEM-EDS images of root and stem cross sections from the four herbaceous plants sampled in the field after incubation in a 200  $\mu$ g/mL PFOA nutrient solution. The bright blue spots represent signals of fluorine (F). The experimental results obtained by SEM-EDS were repeated at least twice with

independent biological samples. **c** The two-sided Pearson correlation (no adjustments) between log RCF, log SCF, log LCF, and log TF of *O. rosea* with the octanol-water partition coefficients ( $\log K_{ow}$ ) for the 15 PFAS with available data; the solid line in the first panel serves as visual guides; the error bands in the second, third, and fourth panels represent the 95% confidence level around the mean value of biological replicates ( $n = 3$ , dashed lines); and the correlation coefficient ( $r$ ) and the corresponding significance levels are shown: log SCF ( $p = 1.50 \times 10^{-5}$ ), log LCF ( $p = 6.66 \times 10^{-8}$ ), and log TF ( $p = 1.17 \times 10^{-10}$ ). Source data are provided as a Source Data file.

### The hyperaccumulating ability of *O. rosea* for different PFAS

To the best of our knowledge, *O. rosea* showed the highest TF ever reported for all the PFAS examined. For example, for the most studied PFOA, *O. rosea* (4.67) demonstrated much higher TF than those reported in crops (0.093–1.08), vegetables (0.20–1.78), and other terrestrial plants (0.08–2.27) (Supplementary Table 9). This disparity is because most plants retain PFAS in roots to mitigate phytotoxicity for

shoots<sup>25–28</sup>, whereas *O. rosea* has evolved hyperaccumulation capabilities through prolonged adaption to contaminated environments studied herein. *O. rosea* also showed high TF values for emerging PFAS that have been rarely investigated, including HFPO-DA (11.6), HFPO-TrA (5.76) and 6:2 FTSA (7.11), and their highest reported TF values were only 3.09<sup>9</sup>, 0.63<sup>6</sup>, and 0.36<sup>29</sup>, respectively. To our knowledge, we reported the first TF measurements for PF4OPeA (4.16), H-PFCA

isomers (3.65–11.6), and other three novel PFAS. Together with the high SCF and LCF values, these findings highlight *O. rosea* as a promising PFAS hyperaccumulator to accumulate and translocate diverse PFAS from contaminated soils.

The varied hyperaccumulating capabilities of *O. rosea* were further explored by correlating the accumulation factors (RCF, SCF, LCF) and TF with the octanol-water partition coefficients ( $\log K_{ow}$ ) of individual PFAS (Fig. 2c).  $\log K_{ow}$ , reflecting compound hydrophobicity, typically increases with the number of perfluorocarbons ( $[CF_2]_n$ ) in PFAS. For the 15 PFAS with available  $\log K_{ow}$  values<sup>40</sup>,  $\log$  RCF displayed a U-shape trend (Fig. 2c), where root accumulation initially decreased with increasing hydrophobicity but rose again for highly hydrophobic PFAS. For instance, the RCF of *O. rosea* for PFCA ( $[CF_2]_nCOO^-$ ) decreased from 3.67 for PFBA (C4) to 1.93 for PFDA (C9) but increased to 2.73 for PFTeDA (C13). This trend is attributed to the combined effects of greater soil retention for long-chain PFAS, reducing their free-dissolved fraction available for root uptake<sup>36</sup>, and their limited translocation to aboveground tissues. This interpretation is supported by the positive correlation of RCF with  $\log K_{ow}$  of PFCA in aquatic plants, unaffected by soil retention<sup>41</sup>, and the negative correlation of  $\log$  SCF,  $\log$  LCF, and  $\log$  TF with  $\log K_{ow}$  in *O. rosea* ( $p < 0.01$ ) (Fig. 2c). Similar trends were also found for other sampled plants (Supplementary Fig. 9).

Moreover, novel PFAS tend to exhibit greater accumulation potential in plants than legacy PFAS. For example, HFPO oligomers and 6:2 Cl-PFESA demonstrated significantly higher accumulation factors than their predecessors, PFOA in fluorochemical production and PFOS in chrome plating, respectively<sup>42,43</sup> (Supplementary Fig. 10). This suggests improved phytoremediation performance but enhanced ecological risks for these novel PFAS. These findings underscore the significance of chemical structure in governing the accumulation and translocation of PFAS, emphasizing the need for structure-activity relationship studies to predict remediation efficiency.

### Identifying key binding components of *O. rosea* for PFAS

Subcellular analysis identifies PFAS binding sites and properties that enhance soil-to-plant uptake and subsequent translocation to aboveground tissues<sup>36,41</sup>. Herein, the concentrations of  $\sum_{82}$ PFAS and ten significant PFAS (PFBA, PFOA, PFNA, HFPO-DA, HFPO-TrA, HFPO-TeA, PFOS, 6:2 Cl-PFESA,  $\omega$ H-PFBA, and  $\omega$ H-PFNA) were examined at both tissue and subcellular levels in *O. rosea*. Figure 3a shows that  $\sum_{82}$ PFAS levels were higher in bottom (1320.7 ng/g) and middle leaves (1168.4 ng/g) compared to top leaves (558.7 ng/g) and flower (437.1 ng/g), with the number of PFAS detected reducing from 30 to 21 (Supplementary Fig. 11). The preferential accumulation in mature tissues over new and reproductive tissues reflects a physiological strategy to mitigate xenobiotic stress, which is also observed in heavy metal hyperaccumulators such as *Noccaea caerulea* (initially classified as *Thlaspi caerulea*<sup>44</sup>) and *Sedum alfredii*<sup>45</sup>.

Subcellular analysis revealed that the cell wall was the primary binding site for PFAS in both roots and leaves of *O. rosea*, accounting for >50% of the accumulation of  $\sum_{82}$ PFAS and most individual PFAS (Fig. 3b), consistent with previous observations in lettuce (*Lactuca sativa* L.)<sup>6</sup>. The preferential binding of PFAS to cell walls over protoplasts acts as a detoxification strategy, mitigating xenobiotic damages while enabling upward translocation from roots to shoots<sup>21,44</sup>. Further isolation of cell walls identified pectin and hemicellulose as the major binding components, responsible for >75% of root-bound PFAS (Fig. 3b). Although pectin and hemicellulose are known to significantly bind metal ions<sup>46,47</sup>, their key role in PFAS accumulation has never been reported before. FTIR analyses of cell walls incubated in a 200  $\mu$ g/mL PFOA solution showed spectral shifts, corresponding to functional groups in pectin and hemicellulose, towards larger wavenumbers at 1740–1756  $cm^{-1}$  (C=O stretching of alkyl ester), 1240–1250  $cm^{-1}$  (C–O stretching), 1152–1164  $cm^{-1}$  (glycoside bond vibrations, O–C–O), and

1049–1067  $cm^{-1}$  (C–O/C–H stretching) (Fig. 3c; Supplementary Table 10). These characteristic peaks disappeared upon removal of pectin and hemicellulose, further validating their critical role in PFAS binding.

The major biological molecules in pectin and hemicellulose (structural configurations in Supplementary Fig. 12) were then quantified to further explore their association mechanism with PFAS. Pectin, the most active component in cell walls, consisted of slightly larger proportion of uronic acid (mainly galacturonic acid in dicotyledonous plants such as *O. rosea*<sup>48</sup>) over total polysaccharides (denoted as total sugar) in *O. rosea* (Fig. 3d). Hemicellulose, a complex heterogeneous polysaccharide, was arbitrarily fractionated into hemicelluloses 1 and 2 using weak and strong alkali (SI-8), respectively. GC-MS analyses revealed that glucose, galactose, and xylose were the predominant monosaccharides in pectin and the two hemicellulose fractions (Supplementary Table 11). The association of PFOA with the four major biological molecules—galacturonic acid, glucose, galactose, and xylose—was characterized by <sup>13</sup>C-NMR, which showed clear shifts in the carboxylate group ( $COO^-$ ) signal peak from –159.18 ppm in pure PFOA to –159.03/159.04 ppm when bound to these molecules (Fig. 3e). In contrast, no peak shifts were observed for the perfluorocarbon chain ( $[CF_2]_n$ ) of PFOA (Supplementary Fig. 13). The interaction of PFOA through  $COO^-$  is likely mediated by H-bonding with the hydroxyl group (–OH) of biological molecules, which was further verified by the calculated free energy of association ( $\Delta G$ , kcal/mol) using density functional theory. The  $\Delta G$  for the association of galacturonic acid, glucose, galactose, and xylose with PFOA through  $COO^-$  was 1.52–5.88 kcal/mol (Fig. 3f), significantly lower than those involving perfluorocarbon chain (7.29–9.75 kcal/mol). Each 1.36 kcal/mol of  $\Delta G$  corresponds to one log unit of the thermodynamic partition coefficient,  $K$ , at 298.15 K. The mechanism of H-bonding was supported by the close distances (1.77–1.85 Å) between O in  $COO^-$  (PFOA) and H in –OH (biological molecules). The slightly positive magnitude of  $\Delta G$  indicates a moderate association, which ensures PFAS accumulation in the cell wall while enabling their uptake from soil to roots and subsequent transport from roots to shoots. However, elucidating the mechanism and modification sensitivity of these key binding components—which determine the hyperaccumulation capacity of *O. rosea*—requires comparative transcriptomics analyses with non-hyperaccumulating populations.

### The hyperaccumulating mechanism of *O. rosea* to PFAS

Unlike the hyperaccumulating *O. rosea* population (denoted as HOR), most previously studied plants, including lettuce (*Lactuca sativa* L.), soybean (*Glycine max* L. Merrill), and pumpkin (*Cucurbita maxima* L.), primarily retain PFAS in roots with limited translocation to shoots<sup>6,27,29</sup>. This contrast prompts investigation into physiological and molecular mechanisms of HOR roots that enable PFAS hyperaccumulation, particularly in comparison to non-hyperaccumulating *O. rosea* populations (NOR) from uncontaminated areas.

Owing to trace levels of PFAS in the background soil ( $\sum_{82}$ PFAS = 0.72 ng/g, Supplementary Fig. 14), the collected NOR contained minimal inherent PFOA contamination (0.27 ng/g in roots, 0.15 ng/g in shoots) compared to HOR (54.9 and 226.2 ng/g). After 7-day hydroponic cultivation with 200 ng/mL PFOA (Supplementary Table 12), HOR showed no growth inhibition compared to untreated controls (CK), whereas NOR displayed a pronounced stress response (Supplementary Fig. 15), signifying domestication of HOR through prolonged PFAS exposure. PFOA accumulation was slightly but significantly ( $p < 0.05$ ) higher in NOR roots (886.9 ng/g) than HOR (662.8 ng/g) (Fig. 4a). In contrast, shoot accumulation of PFOA in NOR (220.3 ng/g) was less than 10% of that in HOR (2456.1 ng/g), resulting in TF of 0.25 and 3.71, respectively. Note that the inherent PFOA, accumulated by NOR and HOR from the natural environment prior to the

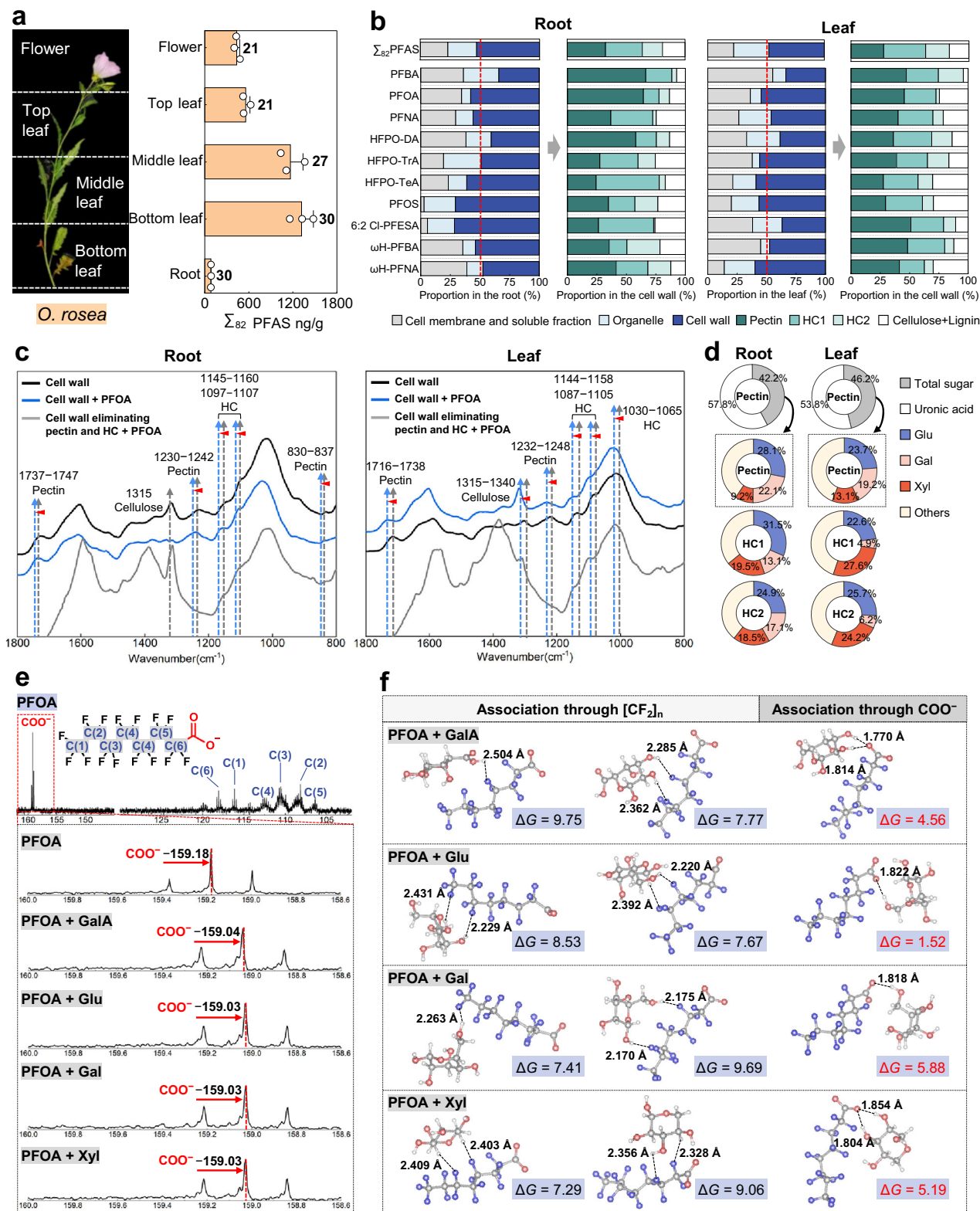
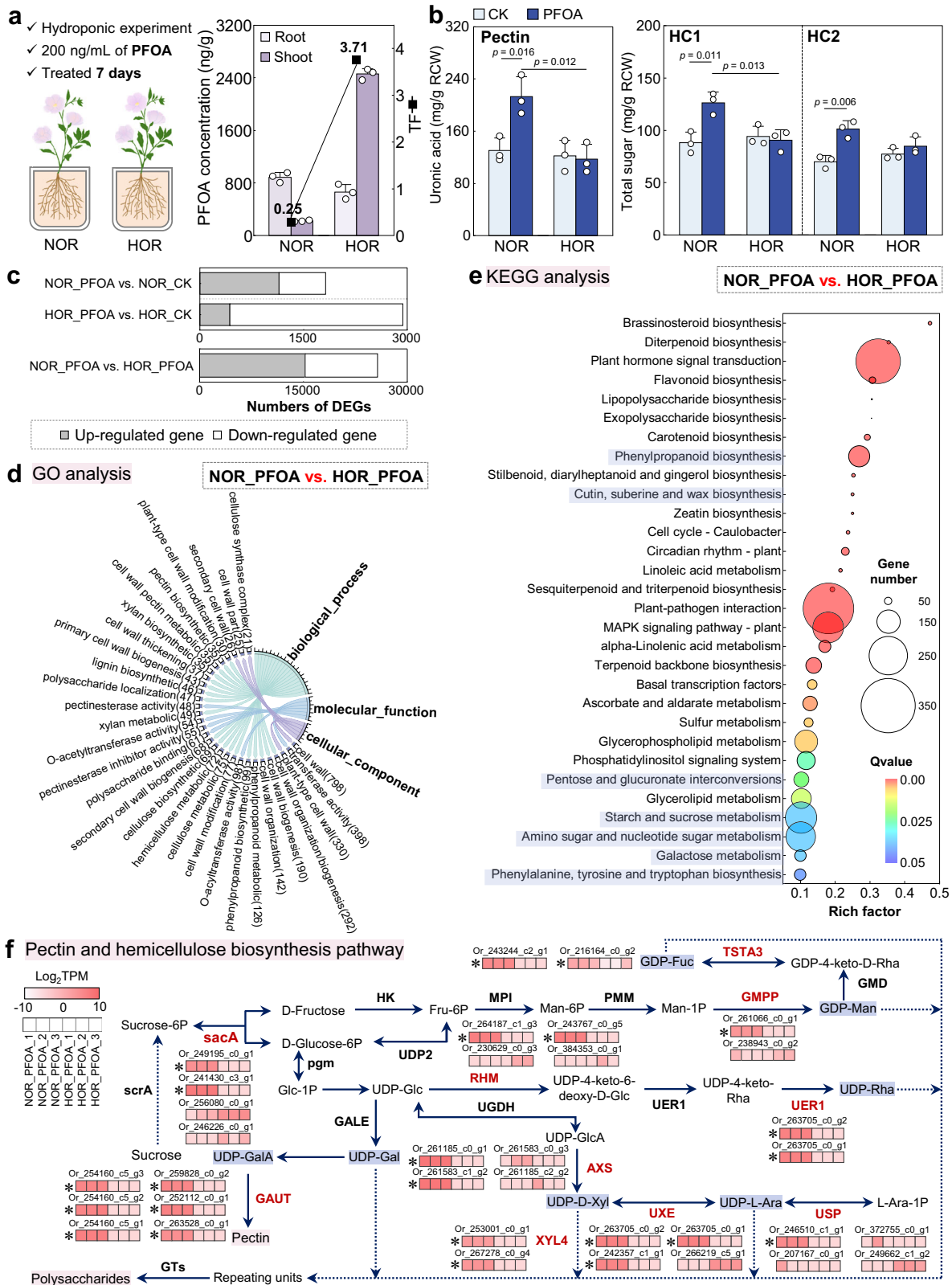


**Fig. 3 | Binding sites of PFAS in hyperaccumulator *O. rosea*.** **a** Concentration of  $\Sigma_{82}$ PFAS in different organizational parts of *O. rosea* and the number of PFAS detected. **b** Proportions of PFAS bound to subcellular fractions (cell wall, organelle, cell membrane and soluble fraction) in roots and leaves of *O. rosea* and to further isolated components in cell walls (HC1 and HC2 refer to hemicellulose 1 and hemicellulose 2, respectively). **c** FTIR spectra of root and leaf cell wall extracted from non-PFAS supplied *O. rosea* (Cell wall), root and leaf cell wall extracted from PFOA (200  $\mu$ g/mL) supplied *O. rosea* (Cell wall + PFOA), root and leaf cell wall extracted from PFOA (200  $\mu$ g/mL) supplied *O. rosea* but eliminating pectin and hemicellulose (Cell wall eliminating pectin and HC + PFOA). **d** Major biological

molecules in the isolated pectin and HC by GC-MS (Glu, Gal, and Xyl refer to glucose, galactose, and xylose, respectively; others refer to the total of arabinose, mannose, fucose and rhamnose). **e**  $^{13}C$  NMR spectra for PFOA and its mixtures with GalA, Glu, Gal and Xyl. **f** The free energy ( $\Delta G$ , kcal/mol) of association between PFOA and the four polysaccharides through  $[CF_2]_n$  and  $COO^-$  in PFOA, with the distance ( $\text{\AA}$ ) of H-bonding ( $H \cdots F$ ,  $H \cdots O$ ) indicated. The calculation was performed at the M06-2X/def2-TZVPP/SMD // M06-2X/6-311 G(d,p)/IEFPCM level of theory. Data in (a) are represented as mean  $\pm$  SD of biological replicates ( $n = 3$ ). Source data are provided as a Source Data file.



hydroponic experiment, has been subtracted. The results demonstrate that enhanced PFAS translocation is an evolved trait specific to HOR, whereas NOR retains exogenous PFAS in roots to protect shoots<sup>49,50</sup>. The ~80% consistency between hydroponic and field-observed TF in HOR supports PFAS uptake from soil to shoots rather than atmospheric absorption, with the marginally lower hydroponic TF attributable to the shorter cultivation period.

The distinct TF values in NOR and HOR indicate divergent root modifications in response to PFOA exposure. Consistent with field samples, the cell wall remained the primary subcellular binding site for PFOA in both populations after hydroponic cultivation, comprising 61.2% (NOR) and 54.7% (HOR) of the total root cellular burden (Supplementary Fig. 16a). The key binding components (pectin and hemicellulose) increased significantly in NOR following PFOA exposure

**Fig. 4 | The hyperaccumulating mechanism of *O. rosea* for PFAS.** **a** PFOA concentrations in the root and shoot of *O. rosea* and the corresponding TF for the non-hyperaccumulating (NOR) and hyperaccumulating populations (HOR) after cultivation in a 200 ng/mL PFOA nutrient solution for 7 days; the reported values have subtracted the inherent PFOA accumulated by HOR and NOR in their original environment. **b** Concentrations of uronic acid and total sugar in the root cell of NOR and HOR to represent changes in pectin and hemicellulose (HC) levels after cultivation of PFOA compared to the control blank (CK). The  $p$  values from independent  $t$ -test (two-tailed, no adjustments) are shown above paired columns. For pectin uronic acid concentrations between different treatments:  $p = 0.016$  for NOR\_CK vs. NOR\_PFOA,  $p = 0.012$  for NOR\_PFOA vs. HOR\_PFOA; for HC1 total sugar concentrations between different treatments:  $p = 0.011$  for NOR\_CK vs. NOR\_PFOA,  $p = 0.013$  for NOR\_PFOA vs. HOR\_PFOA; for HC2 total sugar concentrations between different treatments:  $p = 0.006$  for NOR\_CK vs. HOR\_CK. **c** Number of up- and down-regulated differentially expressed genes (DEGs) in NOR and HOR roots under

PFOA treatment compared to CK (NOR\_PFOA vs. NOR\_CK and HOR\_PFOA vs. HOR\_CK); and the comparison between NOR and HOR (NOR\_PFOA vs. HOR\_PFOA). **d** The top 30 processes identified by GO analysis using the upregulated DEGs in NOR roots compared to HOR, with the gene counts provided in parentheses. **e** The top 30 enriched pathways identified by KEGG analysis in NOR roots compared to HOR, with the 7 pathways involved in root cell wall synthesis shaded in purple. **f** The proposed cell wall pectin and hemicellulose biosynthesis pathways in plant roots, with the expression levels of each unigene encoding the enzymes involved in each step. Colors represent the value of  $\log_2$ TPM from three replicates. The  $p$  values were obtained through statistical testing using a generalized linear model based on the negative binomial distribution (DESeq2), followed by multiple comparison correction. A significance threshold of  $*p < 0.05$  was applied, with specific  $p$  values and detailed gene descriptions are provided in Supplementary Table 17. Data in (**a**, **b**) are represented as mean  $\pm$  SD of biological replicates ( $n = 3$ ). Source data are provided as a Source Data file.

compared to CK ( $p < 0.05$ , Fig. 4b), a signature of cell wall expansion that was absent in HOR. Accordingly, PFOA accumulation in NOR cell walls (2535.1 ng/g) exceeded that in HOR (2018.9 ng/g) ( $p < 0.05$ , Supplementary Fig. 16b). However, the 25% difference in PFOA retention cannot fully explain the substantial lower TF in NOR (0.25) compared to HOR (3.71). Additional modifications of biological components (such as demethylation of pectin<sup>47</sup> and *O*-acetylation of hemicellulose<sup>51</sup>) and their enhanced binding affinity for PFOA likely contribute to TF divergence. Nevertheless, the results support that the domesticated HOR population undergoes less cell wall modifications in response to PFOA, thereby facilitating more efficient upward translocation compared to NOR.

The sensitivity of NOR and HOR roots to PFOA was further explored by RNA-seq analysis, which identified differentially expressed genes (DEGs) in PFOA-treated plants versus CK (Fig. 4c; Supplementary Figs. 17,18 and Tables 13,14). NOR exhibited substantially more upregulated DEGs (1143) than HOR (435). GO enrichment analysis revealed 168 upregulated genes in NOR associated with cell wall synthesis and modifications, particularly, pectin and hemicellulose biosynthesis (e.g., *GAUT*, *XYL4*) based on KEGG metabolic pathway analysis (Supplementary Figs. 19, 20 and Table 15). On the other hand, HOR showed only 35 such genes, with no significant differences from CK in KEGG analysis. These transcriptomic results demonstrated that NOR exhibits both an enhanced cell wall response to PFOA and elevated metabolic activity, consistent with defensive strategies observed in other plants (e.g., *Triticum aestivum* L.<sup>52</sup>, *Leersia hexandra* Swartz<sup>53</sup> and *Oryza sativa* L.<sup>54</sup>) under pollutant stress. The absence of such a biological response in HOR suggests that exposure to 200 ng/mL PFOA may be insufficient to activate its protective mechanisms or induce root cell wall modifications. This observation is consistent with the metal hyperaccumulator *Arabidopsis halleri*<sup>55</sup>, which expresses high levels of metal transporters and metal-chelating enzymes without significant changes in gene expression under metal stress. This finding validates that the pre-adapted genetic traits, rather than induced stress responses, underlie the hyperaccumulator phenotype.

To further identify metabolic processes associated with hyperaccumulation, we compared DEG expression between NOR and HOR under PFOA treatment. This revealed 15,238 upregulated DEGs in NOR relative to HOR (Fig. 4c), including 4817 DEGs associated with cell wall synthesis (56 processes, Supplementary Table 16). The cellular component “cell wall” contained the highest number of DEGs (798), but 19 of the top 30 enriched processes were biological, including cell wall biogenesis and organization. At the molecular functional level, “*O*-acyltransferase activity” and “polysaccharide binding” were predominant (Fig. 4d). KEGG analysis further identified 7 of the top 30 enriched pathways in NOR roots as cell wall metabolism-related (Fig. 4e). In particular, pectin and hemicellulose biosynthesis pathways (e.g., *URI*, *XYL4*, and *GAUT*) were significantly upregulated based on  $\log_2$ TPM values (Fig. 4f; Supplementary Table 17). This pronounced

transcriptional response in NOR reinforces its enhanced root cell sensitivity to PFOA, aligning with the observed increases in pectin and hemicellulose contents and root PFOA retention. In contrast, the non-activated root cell wall response in HOR facilitates efficient PFAS upwards translocation. Such insensitivity to exogenous stress reflects the hyperaccumulating phenotype of the identified *O. rosea*, resulting from decade-long adaptive selection.

Beyond cell wall modifications, the hyperaccumulation of HOR may also involve enhanced symplastic transport and rapid xylem loading, as reported in arsenic- and cadmium- hyperaccumulators<sup>35,56,57</sup>. The synergistic mechanisms enabling PFAS translocation from soil to shoots in *O. rosea* warrant further in-depth investigation.

#### Effectiveness of soil PFAS phytoremediation by *O. rosea*

The remediation potential of *O. rosea* was assessed by calculating the annual remediation efficiency (ARE, %) using SCF and LCF values and plant biomass (Eq. 5). For the ten concentration-significant PFAS, *O. rosea* showed ARE of 5.40–66.6% (Fig. 5a; Supplementary Table 18), corresponding to effective remediation periods of 2–29 years to achieve 80% of PFAS removal from soil (Fig. 5b; Supplementary Table 19). These ARE values were comparable to that reported for the cadmium hyperaccumulator (*S. alfredii*, 17.8%)<sup>21</sup> and directly rely on PFAS translocation efficiency in *O. rosea*. Compounds with higher SCF (25.8) and LCF (85.8) values, such as  $\omega$ H-PFBA, showed the shortest effective remediation period (2 years).

The ARE of field-collected *O. rosea* (HOR) for PFOA was 15.7%, corresponding to an effective remediation period of 9 years for moderately contaminated soil (16.3 ng/g). Elevated contamination levels may impair the accumulation and translocation capabilities of *O. rosea*. In controlled pot experiments with soil PFOA from 50 to 2000 ng/g PFOA, shoot PFOA accumulation increased from 339.42 to 6855.7 ng/g (background-subtracted) over 60 days, accompanied by reducing soil PFOA levels (Fig. 5c). However, HOR exhibited growth inhibition at elevated PFOA exposure, with the harvested biomass (shoots) reducing from 3.05 to 2.35 g (dry weight) per plant (Supplementary Fig. 21). Accordingly, the key accumulation factors declined with increasing soil PFOA: RCF decreased from 2.30 to 1.65, shoot concentration factor (SHCF) from 8.47 to 4.32, and TF from 3.69 to 2.63 (Fig. 5d). These results indicate that elevated soil PFAS negatively affect both plant growth and hyperaccumulation capability, thereby compromising remediation potential. *O. rosea* is thus more effective for lightly to moderately PFAS-contaminated soils, which are commonly encountered near fluorochemical facilities (3–500 ng/g, Supplementary Table 8). The short cultivation time may also contribute to the slightly lower pot-derived TF (3.69, soil PFOA of 50 ng/g) compared to field observations (4.67). The close agreement between these values indicates minimal foliar PFAS uptake from the atmosphere in the field *O. rosea*, reinforcing that shoot accumulation is primarily driven by root translocation.

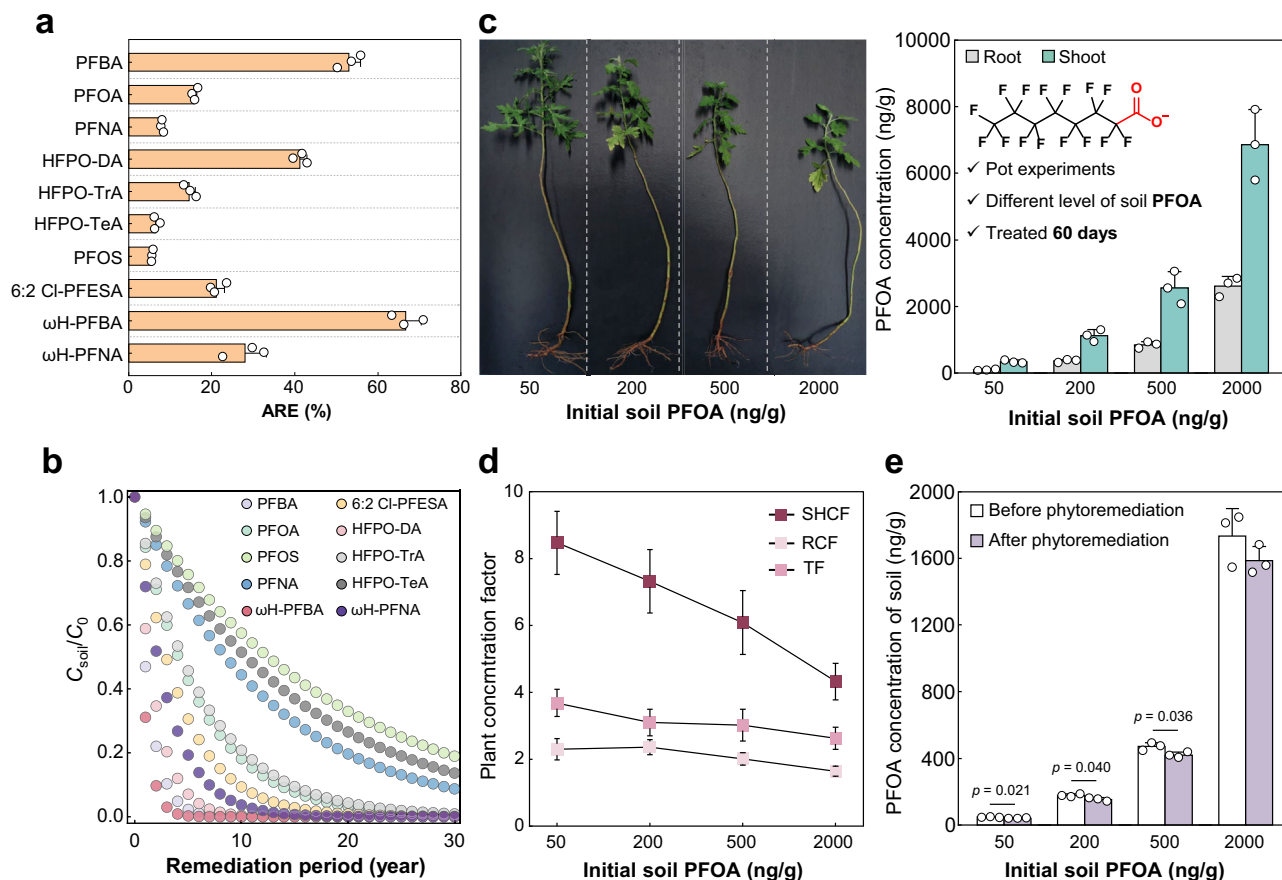


**Fig. 5 | Effectiveness of soil PFAS phytoremediation by *O. rosea*.** **a** The annual remediation efficiency (ARE, %) of *O. rosea* for the 10 concentration-significant PFAS in the sampled soil. **b** The simulated decay of PFAS in contaminated soil ( $C_{\text{soil}}/C_0$ ) along with different remediation periods by *O. rosea*. **c** Morphologies of *O. rosea* and PFOA concentrations in roots and shoots after 60-day cultivation during pot experiments at different soil PFOA levels (50–2000 ng/g). **d** The corresponding

shoot concentration factors (SHCF), RCF, and TF of *O. rosea* for PFOA. **e** Soil PFOA concentrations before and after cultivation of *O. rosea* for 60 days with  $p$  values from independent  $t$ -test (two-tailed, no adjustments) shown above paired columns. The reported values have subtracted inherent PFOA levels accumulated in *O. rosea* from the original environment. Data in (a, c, d, e) are represented as mean  $\pm$  SD of biological replicates ( $n = 3$ ). Source data are provided as a Source Data file.

### Life cycle assessment of phytoremediation coupled with biomass pyrolysis

To assess the potential for integrating phytoremediation with value-added biomass treatment (Fig. 6a), we quantitatively evaluated pyrolysis of field-collected *O. rosea* for PFAS removal and biochar production. Pyrolysis at 300, 500, 700, and 900 °C for 2 h yielded biochar at production rates of 56.8%, 32.8%, 32.4%, and 31.6%, respectively (Supplementary Fig. 22a). Temperature exceeding 500 °C eliminated 99.2% PFAS in *O. rosea*, reducing residual  $\sum_{82}$ PFAS content to 7.85 ng/g (Fig. 6b). Conversely, total fluorine content increased from 9.51  $\mu\text{g/g}$  in raw biomass to 26.5  $\mu\text{g/g}$  in biochar (Supplementary Fig. 22b), suggesting the presence of untargeted PFAS or fluorinated byproducts. Owing to the lack of PFAS standards, we conservatively compared the produced biochar against national combustion standards for low-quality coal with total fluorine limit of 200  $\mu\text{g/g}$ <sup>58</sup>. The biochar also met all quality thresholds for ash, sulfur, calorific value, and heavy metal leaching potential (details in Supplementary Tables 20 and 21). These results demonstrate that pyrolysis at 500 °C effectively eliminates PFAS from harvest biomass while producing environmentally compliant biochar suitable for secondary applications. To comprehensively evaluate this phytoremediation-pyrolysis approach, we conducted LCA and compared its environmental impacts with conventional remediation technologies: soil washing<sup>59</sup> and magnetic activated carbon combined with hydrothermal alkaline (MAC + HALT)<sup>60</sup>.

To facilitate systematic comparison of remediation technologies through LCA, we established a functional unit representing 80% PFOA

removal from 1 hectare of soil with an initial contamination level of 10 ng/g. This reflects the median level observed in agricultural soils near fluorochemical facilities (Supplementary Table 8). Successful remediation would achieve a target PFOA concentration of 2.0 ng/g, meeting the threshold (2.05 ng/g) derived from enforceable drinking water limits set by the U.S. EPA (details in SI-13). A 9-year phytoremediation period is required using the field-observed ARE (15.7%) of *O. rosea* for PFOA. Thus, the “cradle-to-grave” system boundary includes the complete 9-year phytoremediation process, pyrolysis treatment of harvested biomass, and utilization of all pyrolysis products (bio-oil, biogas, and biochar) (Fig. 6a). Further details on the process simulations are provided in SI-14 (Supplementary Figs. 23,26 and Table 23), with complete LCA data (all inputs/outputs) provided in separate Supplementary Data 2.

The LCA revealed significantly lower environmental impacts across 18 categories for the phytoremediation-pyrolysis approach compared to soil washing and MAC + HALT (Fig. 6c; Supplementary Fig. 25). Among these impact categories, global warming potential (GWP) and fossil resource scarcity (FFP) are particularly critical indicators for evaluating remediation sustainability. The GWP values for soil washing and MAC + HALT were 21.0 and 59.9 kg CO<sub>2</sub>/m<sup>2</sup>, respectively, while the FFP values were 6.04 kg and 14.0 kg oil/m<sup>2</sup>. The substantial GWP and FFP values for soil washing are primarily attributed to the washing process, which consumes significant amounts of water and electricity<sup>59</sup>. PFAS removal by MAC accounts for the largest contribution (89.7% and 90.4%) to the extensive GWP and FFP values for

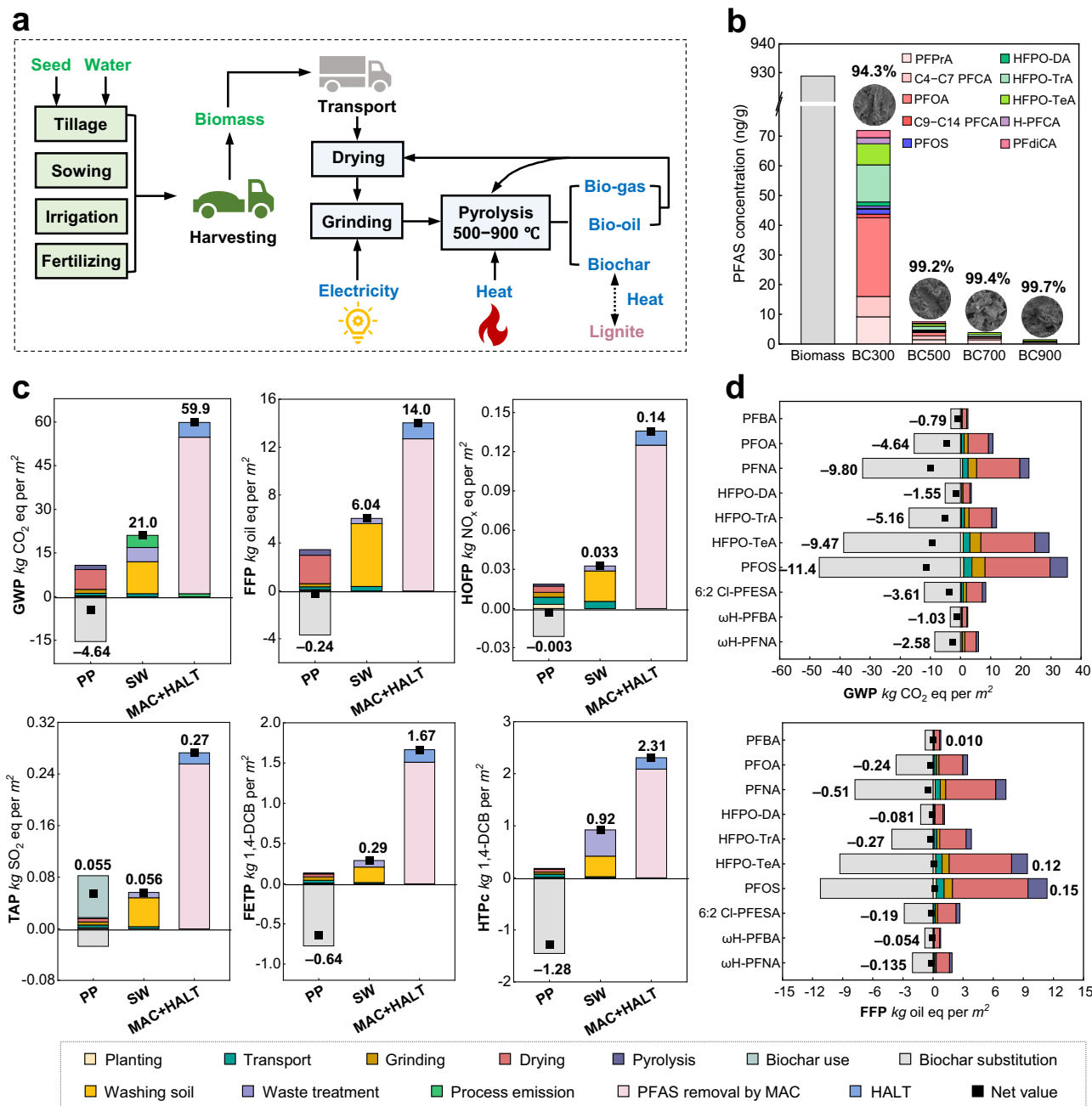


**Fig. 6 | Utilization of hyperaccumulator *O. rosea* biomass and life cycle assessment of phytoremediation.** **a** System boundary of phytoremediation coupled with biomass pyrolysis for LCA. **b** Residual PFAS levels in the biochar (BC) produced from pyrolysis of *O. rosea* biomass at different temperatures, with the removal efficiency for  $\sum_{82}$ PFAS provided above the bars. **c** Comparison of LCA results among phytoremediation plus pyrolysis (PP), soil washing (SW), and magnetic activated carbon plus hydrothermal alkaline (MAC + HALT). The

environmental impact categories compared include GWP global warming potential, FFP fossil resource scarcity, HOPP Ozone formation, Human health, TAP Terrestrial acidification, FETP Freshwater ecotoxicity, HTPc Human carcinogenic toxicity, with the results of the other 12 categories provided in Supplementary Fig. 25. **d** Comparison of GWP and FFP results of phytoremediation plus pyrolysis for different PFAS. Source data are provided as a Source Data file.

MAC + HALT, which is attributed to the substantial consumption of chemicals during the MAC preparation<sup>60</sup>.

In contrast, the net GWP and FFP values for phytoremediation-pyrolysis were both negative at  $-4.64$  kg CO<sub>2</sub>/m<sup>2</sup> and  $-0.24$  kg oil/m<sup>2</sup>, respectively. The net negative GWP and FFP are mainly due to the use of biochar, produced from pyrolysis of harvested *O. rosea*, as a heating source substitute for lignite, which offset 15.4 kg CO<sub>2</sub>/m<sup>2</sup> of GWP and 3.69 kg oil/m<sup>2</sup> of FFP. Conversely, drying *O. rosea* with high water content (up to 85.6%) contributed 63.2% (GWP) and 68.7% (FFP) to the positive emissions. When normalized to per ton of

contaminated soil, phytoremediation-pyrolysis exhibited a GWP of  $-17.9$  kg CO<sub>2</sub>/ton soil, which substantially outperforms previous reported electrothermal processes (130 kg CO<sub>2</sub>/ton soil)<sup>61</sup>. These results underscore the environmental advantages of phytoremediation-pyrolysis, particularly in reducing carbon emissions and fossil resource consumption. The offset by biochar substitution for solid fuel was particularly evident for freshwater ecotoxicity (FETP) and human carcinogenic toxicity (HTPc), resulting in the large negative values of  $-0.641$  kg 1,4-DCB/m<sup>2</sup> and  $-1.28$  kg 1,4-DCB/m<sup>2</sup>, respectively. In addition, burning biochar produced from plant biomass

generated nitrogen dioxide (NO<sub>2</sub>) and sulfur dioxide (SO<sub>2</sub>), contributing 59.5% to the terrestrial acidification (TAP) value. The absolute value of TAP for phytoremediation-pyrolysis (0.055 kg SO<sub>2</sub>/m<sup>2</sup>) was comparable to that of soil washing (0.056 kg SO<sub>2</sub>/m<sup>2</sup>) but much lower than MAC+HALT (0.273 kg SO<sub>2</sub>/m<sup>2</sup>). These results demonstrate that integrating effective biomass utilization into phytoremediation not only avoids potential “secondary pollution” but also reduces environmental burdens, aligning with previous LCA findings on phytoremediation for heavy metal-contaminated soils<sup>62–64</sup>.

Environmental impacts of the phytoremediation-pyrolysis system for different PFAS are primarily determined by their accumulation efficiency in *O. rosea* and the minimum pyrolysis temperature required for PFAS elimination. The net GWP for the 10 concentration-significant PFAS was consistently negative, underscoring advantages of using biochar as a substitute heating source. When excluding the negative GWP contributions caused by biochar substitution, the values for ωH-PFBA (2.39 kg CO<sub>2</sub>/m<sup>2</sup>), PFBA (2.44 kg CO<sub>2</sub>/m<sup>2</sup>), and HFPO-DA (3.58 kg CO<sub>2</sub>/m<sup>2</sup>) were the lowest owing to their superior SCF and LCF values, resulting in an effective remediation period of only 2 to 3 years (Fig. 6d). In contrast, the relatively low SCF and LCF values for HFPO-TeA and PFOS led to prolonged remediation periods of 24 and 29 years. This extended duration increases biomass production and raises energy inputs for drying and pyrolysis, resulting in higher positive GWP values of 29.3 kg CO<sub>2</sub>/m<sup>2</sup> for HFPO-TeA and 35.4 kg CO<sub>2</sub>/m<sup>2</sup> for PFOS. Moreover, the elevated pyrolysis temperature (700 °C) required to eliminate PFBA, PFOS and HFPO-TeA caused extra energy consumption. As a net effect, the FFP values for PFBA (0.01 kg oil/m<sup>2</sup>), HFPO-TeA (0.12 kg oil/m<sup>2</sup>), and PFOS (0.15 kg oil/m<sup>2</sup>) were positive compared to other PFAS. The limited remediation performance of *O. rosea* towards PFOS and HFPO-TeA is primarily attributed to its low hyperaccumulation capacity, likely owing to insufficient evolutionary pressure from the low contamination levels in the studies area. Future efforts are needed to identify and screen potential hyperaccumulators for these PFAS in their contaminated environments.

### Exposure risk reduction and future perspectives of phytoremediation

The identification and validation of *O. rosea* as a PFAS hyperaccumulator represents a transformative advancement in addressing global PFAS contamination through high accumulation capacity and practical biomass valorization strategies. The discovered hyperaccumulator demonstrated root-to-shoot TF of 3.07–58.6 for 18 PFAS, surpassing previously reported values in white willow<sup>19</sup>, weeds<sup>20</sup>, and ferns<sup>36</sup> (typically TF < 1) by up to two orders of magnitude. The rapid growth rate of *O. rosea*<sup>65</sup>, strong stress tolerance, and broad geographical distribution across temperate and subtropical regions<sup>66</sup> make it particularly suitable for large-scale soil remediation.

Monte Carlo simulations (10,000 iterations, Fig. 7) demonstrated the effectiveness of *O. rosea*-mediated phytoremediation in mitigating PFOA risks in fluorochemical contaminated soils across seven provinces in China (Supplementary Table 24). The initial monitoring data (2.17–56.8 ng/g, Supplementary Table 8) revealed an exceeding probability of >99% against the U.S. EPA-derived threshold (2.05 ng/g). After 5 years of phytoremediation, the simulated 95% confidence interval of PFOA concentrations substantially decreased to 1.21–2.33 ng/g (Jiangsu) and 0.88–2.11 ng/g (Shandong), with only 11.4% and 3.36% exceeding probability, respectively. However, more contaminated regions such as Fujian province (median PFOA = 21.3 ng/g) required 20 years to achieve ≤5.70% exceeding probability. These findings underscore both the promise of *O. rosea* for PFAS remediation and the critical need to identify additional hyperaccumulators with enhanced capabilities to optimize treatment timelines. The demonstrated

evolutionary adaption of *O. rosea* as a PFAS hyperaccumulator provides compelling rationale for targeted screening of analogous species in historically polluted areas. Globally distributed fluorochemical industrial sites, characterized by decades of PFAS pollution, serve as ideal “natural laboratories” for identifying such hyperaccumulators through evolutionary selection.

While phytoremediation offers an environmentally sustainable remediation approach, its prolonged timeframe presents limitations for severely contaminated sites or commercial valuable land<sup>67</sup>. Our analysis suggests this technology is most appropriate for moderately contaminated soils (<500 ng/g PFAS) and remote areas with minimal redevelopment pressure. To address the time-intensive disadvantages and enhance phytoremediation viability, we propose three key research priorities: (i) identification of more efficient PFAS hyperaccumulators (particularly from historically fluorochemical-contaminated sites); (ii) development of microbial augmentation and genetic engineering approaches to boost PFAS uptake and translocation; and (iii) creation of sustainable, cost-effective methods to utilize harvested biomass.

## Methods

### Materials and sampling sites

Soils and plants near a fluorochemical facility in East China were sampled in October 2023 (Supplementary Fig. 1). PFAS hyperaccumulators were screened in a park 2 km away from the facility by sampling surface soils (0–15 cm) and roots, stems, and leaves of four woody and four herbaceous plants. The bark of woody plants was also collected. Based on its growth cycle, the estimated age of the PFAS hyperaccumulator *O. rosea* at the time of sampling was approximately 200–210 days. The total carbon content of the sampled soils is provided in Supplementary Table 1.

### Chemicals and reagents

Ultrapure water (resistivity > 18.2 MΩ·cm, Milli-Q IQ7000) was used in all the experiments. HPLC grade methanol (MeOH) and LC-MS grade acetonitrile (ACN) were obtained from Fisher Scientific (MA, USA). Ammonium acetate solution (BioUltra grade, ~5 M in H<sub>2</sub>O) for instrument analysis and ammonium hydroxide (NH<sub>4</sub>OH) solution were obtained from Sigma-Aldrich (MO, USA). HPLC grade solvents were used for the extraction of soil samples, whereas the LC/MS ones were used to prepare the calibration standards and the mobile phase for instrument analysis. Ammonium acetate (purity > 99.0%) and Supelclean ENVI-Carb powder were purchased from Aladdin (Shanghai, China) and Sigma-Aldrich (MO, USA), respectively. Nitrogen (N<sub>2</sub>) (purity 99.998%) was purchased from Jingong Inc. (Hangzhou, China).

Native standards of PFAS were purchased from Wellington Laboratory (ON, Canada), SynQuest Laboratories (FL, USA), and Sigma-Aldrich (MO, USA), or custom synthesized from Fluobon Surfactant Institute (Beijing, China). The structure of the 82 target PFAS including 12 categories were shown in Supplementary Fig. 2. The information including the name, purity and CAS number of the investigated 82 native PFAS, as well as the corresponding isotope-labeled internal standards were provided in Supplementary Tables 2–4, respectively. The stock solution of native standards containing 78 target PFAS was prepared and stored in MeOH, while the remaining 4 compounds (6:2 FTCA, 8:2 FTCA, 6:2 FTUCA and 8:2 FTUCA) were stored in ACN to avoid unwanted transformation. All the 30 internal standards and recovery surrogates were purchased from Wellington Laboratories and had chemical purity of >98%. The stock solution of internal standards containing 26 isotope-labeled PFAS was prepared and stored in MeOH (PFAS-26IS), while M2 6:2 FTCA, M2 8:2 FTCA, M2 6:2 FTCA, and M2 8:2 FTUCA were stored in ACN (PFAS-4IS) to avoid unwanted transformation. The recovery surrogates including M3PFBA, M3PFPeA, M3PFHxA, M4PFOA, and M4PFOS were stored in MeOH and termed as PFAS-5SS.

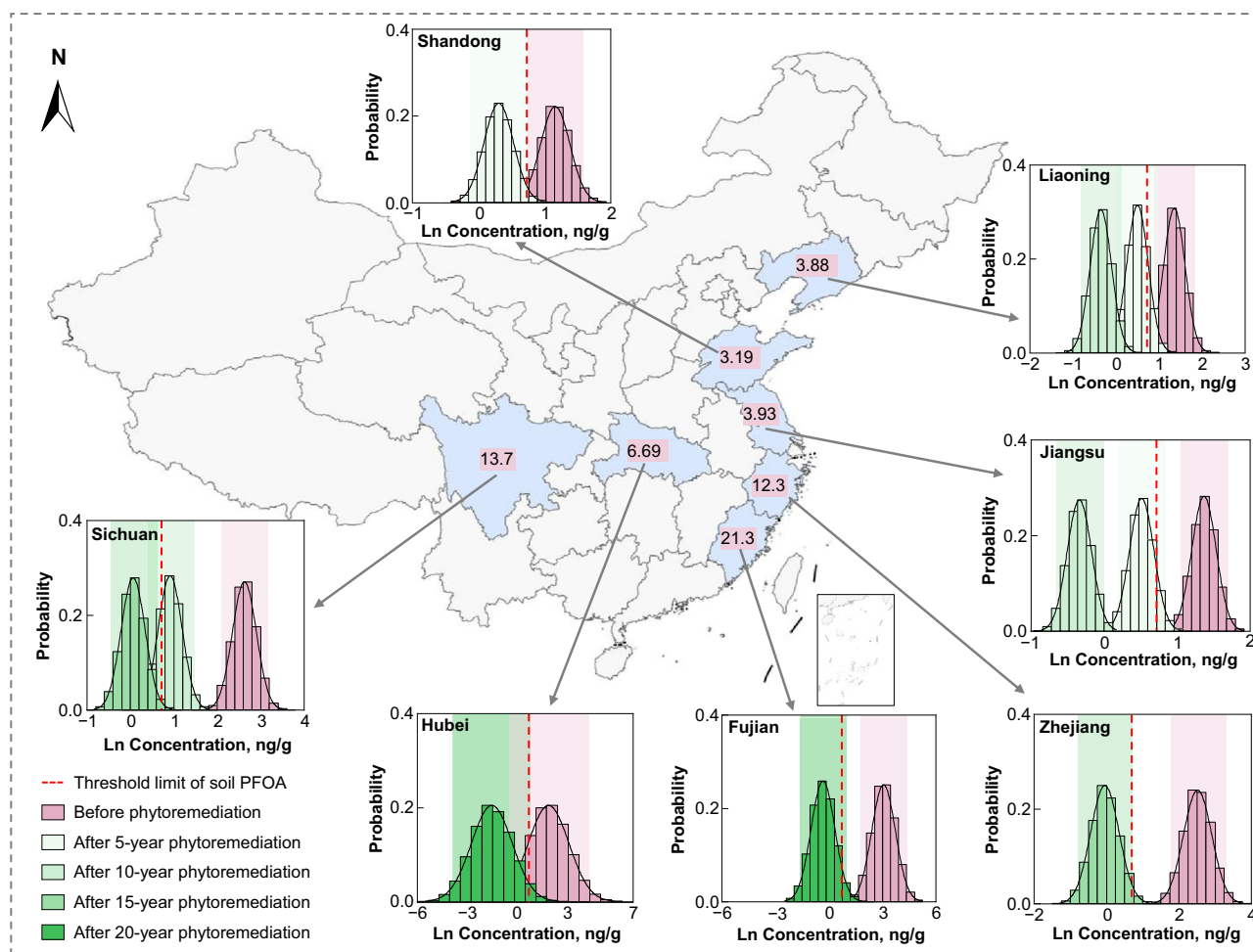


**Fig. 7 | Monte Carlo simulations to indicate the risk mitigation by phytoremediation for the PFOA-contaminated soil near fluorochemical plants in seven provinces of China.** The numbers within the highlighted provinces indicate the 50% confidence interval (CI) of the simulated soil PFOA concentrations (ng/g) before phytoremediation. The black lines indicate the normal distribution curve; the pink and different levels of green shaded areas represent the estimated 95% CI for PFAS levels in the soil before and after 5–20 years of phytoremediation,

respectively, which are compared to the threshold limit of PFOA in soil (red line, 2.05 ng/g, detailed calculations provided in SI-13). The map of China was generated through visualization in R (version 4.3.1), based on a standard map (No. GS (2025) 1508) data obtained from the National Platform for Common Geospatial Information Services of China (<https://www.tianditu.gov.cn/>). Source data are provided as a Source Data file.

### PFAS extraction and analysis in soil and plant samples

The soils were ground with a porcelain mortar and pestle and sieved through a 2 mm stainless steel mesh screen to remove stones and other coarse materials and mixed to obtain homogeneous samples. The harvested herbaceous plants were cleaned by soaking in MeOH/water (1:1, v/v) for 30 min, rinsed with ultrapure water, and then separated into roots, stems, and leaves. The roots, stems, leaves, and bark of woody plants were individually collected after cutting in the field and cleaned by surface-wiping with MeOH/water (1:1, v/v, three times), followed by rinsing with ultrapure water. All soil and plant samples were freeze-dried (FDU-2110, EYELA Co., Japan) for 48 h within a 50 mL polypropylene (PP) tube before extraction and analysis.

Triplicate soil samples (2.00 g) or plants samples (0.050 g) were weighed to 15 mL PP tubes, and then 50  $\mu$ L MPFAC-5SS (20 ng/mL) was spiked before adding 4 mL of extraction solvents. The  $\text{CH}_3\text{COONH}_4$  supplemented MeOH (100 mM) was used as extracting solvent for soil. Four extraction and cleanup methods were compared for plants to guarantee the procedure recovery of PFAS and to reduce the matrix effects, and eventually ammonia/methanol (1:50, v/v) was adopted as the extraction solvent (details in SI-4). The extraction began by vortexing the soil/plant for 3 min and sonicating

for 30 min before centrifugation at 4000 g for 10 min at 22 °C. The supernatant was pipetted out into a new 15 mL PP tube preloaded with 250 mg of ENVI-Carb powder for purification. The aforementioned extraction was repeated twice, and the three extracts (-12 mL) were pooled before centrifugation again (4000 g, 20 min, 22 °C). The supernatant was pipetted out into a new 15 mL PP tube (-12 mL). The ENVI-Carb powder was rinsed twice with 2 mL MeOH. The total extract (-16 mL) was concentrated under a gentle stream of  $\text{N}_2$  at 40 °C to 0.5 mL before transferred into a 1.5 mL EP tube and centrifuged for 20 min at 16,000 g (22 °C). The final supernatant was transferred into a 1 mL PP sample vial and stored at -20 °C before analysis (sample stock). An aliquot of 100  $\mu$ L of sample stock was combined with 10  $\mu$ L of PFAS-26IS (20 ng/mL), 10  $\mu$ L of PFAS-4IS (20 ng/mL), and 80  $\mu$ L of MeOH to make the injection sample. In total, 82 PFAS were quantitatively analyzed by the ultra-high performance liquid chromatography coupled to a Triple Quad™ 6500 plus mass spectrometer (HPLC-MS/MS, SCIEX, MA, USA). Detailed information of the target PFAS and instrument analysis methods are provided in SI-2 and SI-3. Quality control data regarding the limit of detection, spike recoveries, and matrix effects can be found in SI-4. Results of target MS data of PFAS are provided in Supplementary Data 1.

## Data analysis

The root (RCF), stem (SCF), and leaf (LCF) concentration factors as well as the translocation factor (TF) were calculated according to Eq. 1–4.

$$\text{RCF} = C_{\text{root}}/C_{\text{soil}} \quad (1)$$

$$\text{SCF} = C_{\text{stem}}/C_{\text{soil}} \quad (2)$$

$$\text{LCF} = C_{\text{leaf}}/C_{\text{soil}} \quad (3)$$

$$\text{TF} = \frac{C_{\text{shoot}}}{C_{\text{root}}} = \frac{C_{\text{leaf}} \times M_{\text{leaf}} + C_{\text{stem}} \times M_{\text{stem}}}{M_{\text{leaf}} + M_{\text{stem}}} \times \frac{1}{C_{\text{root}}} \quad (4)$$

where  $C_{\text{soil}}$  is the soil PFAS concentration (ng/g dry weight (dw));  $C_{\text{root}}$ ,  $C_{\text{stem}}$  and  $C_{\text{leaf}}$  are the concentrations of PFAS (ng/g dw) in the plant root, stem and leaf, respectively; and  $M_{\text{root}}$ ,  $M_{\text{stem}}$ , and  $M_{\text{leaf}}$  represent the mass (g dw) of plant roots, stems and leaves of herbaceous plants, respectively.  $M_{\text{leaf}}$  and  $M_{\text{stem}}$  cannot be determined for woody plants and were assumed to be the same to calculate TF.

A model contaminated soil<sup>21</sup> was defined as a soil depth of 20 cm, a planting spacing interval of 5 cm × 5 cm, and a bulk density of 1.30 g/cm<sup>3</sup>. The annual remediation efficiency (ARE) towards the model soil by herbaceous plants was calculated as:

$$\text{ARE} (\%) = \frac{C_{\text{leaf}} \times M_{\text{leaf}} + C_{\text{stem}} \times M_{\text{stem}}}{C_{\text{soil}} \times M_{\text{soil}}} \times 100\% \quad (5)$$

where  $M_{\text{leaf}}$  and  $M_{\text{stem}}$  are the biomass of plant leaves and stems (g dw), respectively;  $C_{\text{soil}}$  is the initial soil concentration (ng/g dw); and  $M_{\text{soil}}$  is the mass of the model contaminated soil (g dw).  $M_{\text{leaf}}$  and  $M_{\text{stem}}$  at the time of sampling (October, when annual herbaceous plants complete most of their growth cycle) were used for the calculation of ARE.

## Observation of PFAS in plant roots and stems by SEM-EDS

The collected herbaceous plants (*O. rosea*, *A. calamus*, *S. canadensis* and *E. annuus*) were cultured in a nutrient solution containing 200 µg/mL PFOA for 7 days. Upon harvest, fresh roots (0.2–0.8 mm from the root tip) and stems were cut into 10–15 µm pieces by a freezing microtome (SLEE MTC, Germany). The dehydrated cross-sections were wrapped by a Hitachi Model E-1010 ion sputter for 5 min using gold-palladium and imaged using a Hitachi Model TEM-1000 SEM and INCA100EDS (Oxfordshire, UK).

## Subcellular fractionation and cell wall analysis

The roots and leaves (1.0 g of fresh sample) were respectively mixed and supplemented with 20 mL of extraction solution before ground into a homogenate in a mortar on an ice bath<sup>6</sup>. The extraction solution was composed of a mixture of 50 mmol/L Tris HCl buffer (pH 7.5), 250 mmol/L sucrose, 1.0 mmol/L dithioerythritol, 5.0 mmol/L ascorbic acid, and 1.0% (w/v) polyvinylpyrrolidone. The homogenate was then filtered through a 70 µm nylon cloth, and the residue was the cell wall portion. The filtrate was centrifuged at 10,000 g for 30 min at 4 °C (Model ALLEGRA-64R, Beckman Coulter, Inc. USA), and the precipitate was the organelle fraction. The supernatant consisted of cell membrane and soluble fraction (mainly including cytoplasm, organic matter, inorganic ions, and macromolecules in vacuoles).

Pectin and hemicellulose in the cell wall were extracted by hot water and alkaline solution, respectively<sup>47</sup>. Briefly, the cell walls obtained through subcellular fractionation were freeze-dried for 24 h, and then 20–30 mg of the cell walls were placed in a 2 mL centrifuge tube. One mL of distilled water was added, and the mixture was heated in a 100 °C water bath for 1 h. The supernatant was collected by centrifugation, and this process was repeated three times. All supernatants collected were designated as pectin. Then, one mL of a mixed

solution containing 0.1% NaBH<sub>4</sub> and 4% KOH (weak alkali) was added. After 12 h, the supernatant was collected by centrifugation, and this step was repeated twice. All supernatants collected were designated as hemicellulose 1 (HC1). Finally, one mL of a mixed solution containing 0.1% NaBH<sub>4</sub> and 24% KOH (strong alkali) was added. After 12 h, the supernatant was collected by centrifugation, and this step was repeated twice. All supernatants collected were designated as hemicellulose 2 (HC2). The content of PFAS in different fractions was extracted and analyzed, and the contributions were reported against the dry weight of each fraction.

Using galacturonic acid (Sigma) as a standard, uronic acid concentrations were determined according to *Blumenkrantz and Asboe-Hansen*<sup>68</sup>. Briefly, 200 µL of pectin extracts were placed into 1.5 mL centrifuge tubes, and then 1 mL of 98% H<sub>2</sub>SO<sub>4</sub> containing 0.0125 M Na<sub>2</sub>B<sub>4</sub>O<sub>7</sub>·10H<sub>2</sub>O was added. After boiling in 100 °C water for 5 min, the solution was cooled immediately on ice, and then M-hydro-diphenyl dissolved in 0.15% NaOH was added to the tube rapidly. After incubation at room temperature for 20 min, the absorbance value was measured at 520 nm spectrophotometrically.

The total sugar content in pectin and hemicellulose were determined using phenol sulfuric acid method<sup>69</sup>. Briefly, 200 µL of HC1 and HC2 extracts were pipetted into a 2 mL centrifuge tube, and then 10 µL of phenol solution and 1 mL of concentrated sulfuric acid were added. The solution was kept at room temperature before being heated in a 100 °C water bath for 20 min. Then, the solution was immediately cooled on ice before determining the absorbance spectrophotometrically at 490 nm. The calibration curve for total sugar was prepared by pipetting 0, 20, 50, 100, 150, and 200 µL of 0.1 µg/µL glucose solution and adjusting to 200 µL with ultrapure water. The total sugar concentrations were reported as glucose equivalents.

The content of monosaccharides, including glucose, galactose, xylose, arabinose, mannose, fucose, and rhamnose, in pectin and hemicellulose was determined by GC-MS (GCMS-QP2010 Plus, Shimadzu Corporation, Japan). Briefly, the supernatants of root extracts by hot water (targeted to extract pectin), 4% (targeted to extract HC1) and 24% KOH (targeted to extract HC2) were neutralized to pH 7 by acetic acid, before dialyzing for 48 h (replace the distilled water every 2 h). The resulting samples were acid-hydrolyzed to obtain monosaccharides, adding 800 µL of H<sub>2</sub>O, followed by reduction with 0.4 mL of 10% NaBH<sub>4</sub> at 40 °C and reaction termination using 800 µL of glacial acetic acid. A 400 µL aliquot was then acetylated with 600 µL methylimidazole and 4 mL acetic anhydride at room temperature. After quenching with 10 mL H<sub>2</sub>O, the derivative was extracted with 3 mL dichloromethane, washed thoroughly with water, dried over anhydrous Na<sub>2</sub>SO<sub>4</sub>, and prepared for analysis. GC-MS analysis was equipped with an Rxi-SMS capillary column (30 m × 0.25 mm × 0.25 µm) using high-purity helium as the carrier gas at a constant flow rate of 1.02 mL/min and a split ratio of 1:30. The oven temperature was initially held at 155 °C for 23 min, increased to 200 °C at 3 °C/min and held for 5 min, and increased to 300 °C at 20 °C/min and held for 2 min. The injection temperature was set at 250 °C, along with an interface temperature at 250 °C. The MS was operated in electron impact ionization mode at 70 eV and at 200 °C, and the data were acquired in selected ion monitoring (SIM) mode.

## FTIR analysis

FTIR analysis (Nicolet 6700 Thermo Fisher Scientific Inc., MA, USA) was carried out in three series of samples as follow: root and leaf cell wall extracted from non-PFAS supplied *O. rosea*, root and leaf cell wall extracted from PFOA (200 µg/mL) supplied *O. rosea*, and root and leaf cell wall extracted from PFOA (200 µg/mL) supplied *O. rosea* but eliminating pectin and hemicellulose. The pectin and hemicellulose in the cell wall were removed by hot water and alkaline solution, respectively, following the extraction procedure described in the **Subcellular fractionation and cell wall analysis** section. Changes of

surface functional groups were identified through FTIR analysis with 50 scans being taken at  $2\text{ cm}^{-1}$  resolutions within the range of  $800\text{--}1800\text{ cm}^{-1}$ .

### NMR analysis

Solution NMR spectrum was recorded by a 600 MHz solution NMR spectrometer (Bruker BioSpin, Rheinstetten, Germany) using  $d_4$ -MeOH as the deuterated solvent. Two different preparations were used for NMR analyses: 20 mg of PFOA dissolved in 600  $\mu\text{L}$  of  $d_4$ -MeOH and 20 mg PFOA together with 20 mg of individual galacturonic acid, glucose, galactose, and xylose in 600  $\mu\text{L}$  of  $d_4$ -MeOH. The  $^{19}\text{F}/^{13}\text{C}$  NMR spectra were Fourier transformed, phased and baseline corrected, before further processed and analyzed using the MestReNova 9.0.1 software.

### Density functional theory (DFT) calculations

Quantum mechanical calculations reported in the current work were performed using the Gaussian 16 program suite (Revision C.01) at the standard temperature (298.15 K) and pressure (1 atm)<sup>70</sup>. The geometry optimization of compounds was performed at the M06-2X/6-311 G(d,p)/IEFPCM level of theory. Frequency analysis was conducted to verify the absence of imaginary frequencies for local minima. The more accurate determination of the electronic energy was calculated at the M06-2X/def2-TZVPP/SMD level of theory through single point approach to obtain the free energy of association ( $\Delta G$ , kcal/mol) between PFOA and biological molecules (galacturonic acid, glucose, galactose, and xylose)<sup>71–74</sup>. The  $\Delta G$  values were corrected for the free energy required (1.89 kcal/mol) to convert the molecule from the gas phase standard state (1 atm) to that of the solution phase (1 M)<sup>75</sup>.

### Hydroponic and pot experiments in the lab

Young *O. rosea* plants (aged 40–50 days, pre-bloom) were collected in April 2024 and used for hydroponic and pot experiments. The HOR population was sampled from the same fluorochemical-contaminated site, whereas the uncontaminated NOR population was collected from a background location 150 km away from the facility. For each population and treatment, 36 (hydroponic) and approximately 20 (pot) biological replicates were established. Following treatment completion, relatively healthy and uniformly grown plants were randomly selected for subsequent analyses. The experimental design incorporated three biological replicates for PFAS analysis, polysaccharides concentration measurement, and RNA-seq, with six biological replicates used to determine root length, shoot height, and root/shoot dry biomass.

For hydroponic experiments, the two populations of *O. rosea* were precultured for two weeks in the 1/2-strength Hoagland nutrient solution (details refer to Supplementary Table 14), with continuously aerated and renewed every 3 days. Then, the plants were transferred into a full-strength nutrient solution supplied with 0 (control blank, CK) and 200 ng/mL PFOA and further incubated for 7 days. The NOR and HOR harvested were used to determine PFOA concentrations to compare the TF and for RNA-seq analysis. The hydroponic experiment was designed to validate field-observed TF values for HOR while excluding the interference from soil heterogeneity and atmospheric deposition and to compare cellular and molecular responses between NOR and HOR. The use of a single, relatively high concentration of PFOA is based on its dominance in field samples and reported phytotoxicity thresholds (200–500 ng/mL<sup>6,36</sup>).

For pot experiments, after pre-cultivating the soil with different concentrations of PFOA for 30 days, the HOR and NOR were transplanted and cultivated in a growth chamber. The chamber conditions were set to 14/10 h day/night alternate cycles, with a relative humidity of 70/85% at 26/20 °C, respectively. After 60 days of cultivation with different concentrations of soil PFOA (50, 200, 500 and 2000 ng/g), the RCF, shoot concentration factor (SHCF), TF, and the dry weight of

roots and shoots, were obtained. The concentration gradient established in pot experiments were designed to replicate the realistic soil contamination (27.2–1915.8 ng/g) observed near fluorochemical facilities in this study (Supplementary Table 7), quantify concentration-dependent phytoremediation efficiency, and determine optimal soil PFAS ranges for practical filed application of *O. rosea*.

Specifically, when reporting PFOA concentrations in plant tissues from hydroponic and pot experiments and calculating RCF, SHCF, and TF values, the inherent PFOA concentrations accumulated by HOR and NOR in their original environment were subtracted.

### Transcriptome sequencing (RNA-Seq)

After incubation of *O. rosea* in the nutrient solution containing 200 ng/mL PFOA for 7 days, the total RNA in the roots was extracted according to the instructions of the RNAout columnar plant kit (OMEGA, Beijing, China). The total RNA concentration was quantified using a Qubit 2.0 fluorometer, and the Optical Density (OD) values were measured at 260 nm and 280 nm. RNA integrity and genomic DNA contamination were further assessed via agarose gel electrophoresis. RNA-seq was performed using the Illumina HiSeq 2500 sequencing platform, and RNA-seq data were processed and spliced by the Trinity software. TPM (Transcripts per million) values were used to estimate the gene expression. And DESeq grouping with  $p < 0.05$  as the standard was used to identify the differentially expressed genes (DEGs)<sup>76</sup>. Furthermore, GO (Gene Ontology) gene functional annotation and KEGG (Kyoto Encyclopedia of Genes and Genome) metabolic pathway analysis were performed on genes using Goseq and KOBAS to obtain corresponding annotations for the DEGs, and the identified DEGs were recorded in the GO and KEGG sets.

### Production and characterization of biochar

The collected *O. rosea* biomass near the fluorochemical facility was washed with MeOH/H<sub>2</sub>O (1:1, v/v) to remove the surface adsorbed PFAS, freeze-dried, and then ground into powder and sieved through a 2 mm mesh. Subsequently, 50 g of the biomass powder were weighed and placed in a corundum crucible, which was then put into an atmosphere-controlled box furnace under a N<sub>2</sub> environment. The temperature was programmed to increase at a rate of 5 °C/min to various carbonization temperatures (300 °C, 500 °C, 700 °C, and 900 °C), held for 2 h, and then allowed to cool naturally to room temperature. After cooling, the samples were collected, ground, and sieved (0.25 mm) before storage in a desiccator.

To determine the total fluorine content in the biomass and biochar, the solids (~10 mg) were loaded into a combustion furnace (AQF-2100H, Thermo Scientific, USA) with a temperature of 1100 °C under 400 mL/min oxygen flow before introducing to an ion chromatograph for fluoride analysis (Dionex ICS-2100, Thermo Scientific, USA). The content of C, H, N, S, and O in biochar were determined by an elemental analyzer (Uncube & Shimadzu TOC-L, Elementar, Germany) (Supplementary Table 20). The concentrations of 82 target PFAS in the biomass and biochar were determined following the extraction and cleanup methods of soil samples. Structure and surface characteristics were imaged by a scanning electron microscope (SEM, FEI QUANTA FEG 650), and the surface element analysis was simultaneously performed using energy dispersive X-ray spectroscopy (EDS, EDAX Inc. Genesis XM). The results are provided in Supplementary Fig. 22.

The Toxicity Characteristic Leaching Procedure (TCLP) experiments of the biochar were conducted via adding samples to glacial acetic acid solution (pH  $2.88 \pm 0.05$ ) at a mass/volume ratio of 1:20 and shaking for 18 h. The extracts were diluted fivefold with 1% nitric acid and then filtered. The heavy metal (Zn, Cr, Cu, Pb, Ni, Cd) concentration of the filtrates was determined by inductively coupled plasma mass spectrometer (ICP-MS, ThermoFisher ICAP RQ). The instrument parameters were as follows: Plasma power 1550 W, cool gas flow 14 L/min, auxiliary gas flow 0.8 L/min, nebulizer gas flow 0.95 L/min. Kinetic

energy discrimination (KED) measurement mode with He as a collision gas was used during the analysis. To correct the matrix effect and signal drift, Sc and Ge were used as online internal standard solutions during the analysis. The calibration curve was constructed by measuring the signal intensities of these standard solutions. The samples were aspirated into the ICP-MS, and the Zn, Cr, Cu, Pb, Ni, and Cd concentrations were determined based on the calibration curve. Each sample was analyzed in triplicate, and the average value was reported. The results are provided in Supplementary Table 21.

### Life cycle assessment

LCA was conducted in SimaPro TM (V9.2) to assess the sustainability of *O. rosea*-mediated phytoremediation combined with biomass pyrolysis for PFAS contaminated soil. Two traditional remediation technologies, soil washing and magnetic activated carbon plus hydrothermal alkaline (MAC + HALT), were also assessed for comparison (see SI-14). The functional unit was set to remediate 1 hectare of contaminated soil with initial PFOA concentration of 10 ng/g, with a criterion of 80% removal. ReCiPe2016 (H) was applied in the life cycle impact assessment (LCIA) where 18 environmental impact categories were assessed. Further details of LCA parameters and sensitivity analyses are provided in SI-14.

### Statistics and reproducibility

Unless otherwise specified, all samples were analyzed with at least three independent biological replicates, following standard practices in the field. Data are presented as mean  $\pm$  SD of three biological replicates. Statistical analysis was conducted using the OriginPro 2021 (OriginLab). Differences between groups were primarily analyzed using two-sided, unadjusted independent *t*-tests. Two-sided Pearson's correlation test was employed for correlation analysis. A *p* value of less than 0.05 was considered statistically significant. No data were excluded from the analyses. To ensure unbiased group allocation, the experimental plants were randomly assigned to different treatment groups. Furthermore, the investigators were blinded to group allocation during both the experimental procedures and outcome assessment to prevent assessment bias. The effectiveness of phytoremediation using *O. rosea* to mitigate the health risk of PFOA in surface soils adjacent to fluorochemical facilities was modeled using Monte Carlo simulations (*R* version 4.3.1). The soil PFOA concentration data from seven provinces in China (Liaoning, Shandong, Jiangsu, Zhejiang, Hubei, Fujian, and Sichuan) (Supplementary Table 8), where major fluorochemical plants are distributed, were used to construct the probability distribution dataset for further iterations of 10,000 times. PFOA concentrations after continuous remediation using *O. rosea* for 5, 10, 15, and 20 years in each province were modeled (Supplementary Table 24) by using an ARE of 15.7% (Supplementary Table 18) and compared against the threshold limit of 2.05 ng/g obtained based on the enforceable drinking water limit set by U.S. EPA (details in SI-13). Graphs were generated by OriginPro and PowerPoint.

### Reporting summary

Further information on research design is available in the Nature Portfolio Reporting Summary linked to this article.

### Data availability

The map of China was generated through visualization in *R* (version 4.3.1), based on a standard map (No. GS (2025) 1508) data obtained from the National Platform for Common Geospatial Information Services of China (<https://www.tianditu.gov.cn/>). The raw data of Illumina sequencing have been submitted to the NCBI Sequence Read Archive (SRA) and are accessible under the BioProject accession number PRJNA1334603. The other data generated in this study are provided in the Supplementary Information. Life-cycle assessment inventory data

and raw targeted mass spectrometry data are provided in the Supplementary Data files. Source data are provided with this paper.

### References

1. Evich, M. G. et al. Per- and polyfluoroalkyl substances in the environment. *Science* **375**, 512 (2022).
2. OECD. Working towards a global emission inventory of PFASs: focus on PFASs-status quo and the way forward. United Nations Organisation for Economic Co-operation and Development Environment, Health and Safety Publications Series on Risk Management No 30 (OECD, 2015).
3. Glüge, J. et al. An overview of the uses of per- and polyfluoroalkyl substances (PFAS). *Environ. Sci. Process. Impacts* **22**, 2345–2373 (2020).
4. Cheng, Y. et al. Temporal trends of legacy and emerging PFASs from 2011 to 2021 in agricultural soils of eastern China: impacts of the Stockholm Convention. *Environ. Sci. Technol.* **57**, 9277–9286 (2023).
5. Sheng, N., Pan, Y., Guo, Y., Sun, Y. & Dai, J. Hepatotoxic effects of hexafluoropropylene oxide trimer acid (HFPO-TA), a novel perfluorooctanoic acid (PFOA) alternative, on Mice. *Environ. Sci. Technol.* **52**, 8005–8015 (2018).
6. Chen, L. et al. New insights into the accumulation, transport, and distribution mechanisms of hexafluoropropylene oxide homologues, important alternatives to perfluorooctanoic acid, in lettuce (*Lactuca sativa* L. *Environ. Sci. Technol.* **57**, 9702–9712 (2023).
7. Richardson, M. J. et al. Per- and poly-fluoroalkyl substances in runoff and leaching from AFFF-contaminated soils: a rainfall simulation study. *Environ. Sci. Technol.* **56**, 16857–16865 (2022).
8. Xia, C. et al. The ins and outs of per- and polyfluoroalkyl substances in the Great Lakes: the role of atmospheric deposition. *Environ. Sci. Technol.* **58**, 9303–9313 (2024).
9. Wang, D. et al. Legacy and novel per- and polyfluoroalkyl substances in surface soils across China: source tracking and main drivers for the spatial variation. *Environ. Sci. Technol.* **58**, 20160–20171 (2024).
10. Wu, E. et al. Metabolic and microbial profiling of soil microbial community under per- and polyfluoroalkyl substance (PFAS) stress. *Environ. Sci. Technol.* **57**, 21855–21865 (2023).
11. Zhang, M. et al. Bioaccumulation and human exposure of perfluoroalkyl acids (PFAAs) in vegetables from the largest vegetable production base of China. *Environ. Int.* **135**, 105347 (2020).
12. Hopkins, K. E. et al. Characterizing the movement of per- and polyfluoroalkyl substances in an avian aquatic–terrestrial food web. *Environ. Sci. Technol.* **57**, 20249–20260 (2023).
13. Niu, Q. et al. Aerobic or anaerobic? microbial degradation of per- and polyfluoroalkyl substances: a review. *J. Hazard. Mater.* **480**, 36173 (2024).
14. Li, F. et al. Short-chain per- and polyfluoroalkyl substances in aquatic systems: occurrence, impacts and treatment. *Chem. Eng. J.* **380**, 122506 (2020).
15. Shende, T., Gangadhar Andaluri, G. & Suri, R. Frequency-dependent sonochemical degradation of perfluoroalkyl substances and numerical analysis of cavity dynamics. *Sep. Purif. Technol.* **261**, 118250 (2020).
16. Ahmed, M. B. et al. Advanced treatment technologies efficacies and mechanism of per- and poly-fluoroalkyl substances removal from water. *Process Saf. Environ.* **136**, 1–14 (2020).
17. Juhasz, A. L., Kastury, F., Herde, C. & Tang, W. Application of soil amendments for reducing PFAS leachability and bioavailability. *Environ. Pollut.* **307**, 119498 (2022).
18. Navarro, D. A. et al. Stabilisation of PFAS in soils: long-term effectiveness of carbon-based soil amendments. *Environ. Pollut.* **323**, 121249 (2023).
19. Würth, A. et al. Phytoscreening for per- and polyfluoroalkyl substances at a contaminated site in Germany. *Environ. Sci. Technol.* **57**, 4122–4132 (2023).

20. He, Q. et al. Phytoextraction of per- and polyfluoroalkyl substances (PFAS) by weeds: effect of PFAS physicochemical properties and plant physiological traits. *J. Hazard. Mater.* **454**, 131492 (2023).
21. Guo, X. et al. Integrated glycolysis and pyrolysis process for multiple utilization and cadmium collection of hyperaccumulator *Sedum alfredii*. *J. Hazard. Mater.* **422**, 126859 (2022).
22. Ziegler-Devin, I. et al. Steam explosion pretreatment of willow grown on phytomanaged soils for bioethanol production. *Ind. Crop. Prod.* **140**, 111722 (2019).
23. Ma, L. Q. et al. A fern that hyperaccumulates arsenic. *Nature* **409**, 579 (2001).
24. Yang, X. et al. Cadmium tolerance and hyperaccumulation in a new Zn-hyperaccumulating plant species (*Sedum alfredii* Hance). *Plant Soil* **259**, 181–189 (2004).
25. Yamazaki, E. et al. Residue distribution and daily exposure of per- and polyfluoroalkyl substances in Indica and Japonica rice. *Environ. Sci. Technol.* **57**, 4208–4218 (2023).
26. Shen, L. et al. Characterization of the bioavailability of per- and polyfluoroalkyl substances in farmland soils and the factors impacting their translocation to edible plant tissues. *Environ. Sci. Technol.* **58**, 15790–15798 (2024).
27. Wen, B. et al. The roles of protein and lipid in the accumulation and distribution of perfluorooctane sulfonate (PFOS) and perfluorooctanoate (PFOA) in plants grown in biosolids-amended soils. *Environ. Pollut.* **216**, 682–688 (2016).
28. Krippner, J. et al. Accumulation potentials of perfluoroalkyl carboxylic acids (PFCAs) and perfluoroalkyl sulfonic acids (PFSA) in maize (*Zea mays*). *J. Agric. Food Chem.* **63**, 3646–3653 (2015).
29. Zhao, S. et al. Fate of 6:2 fluorotelomer sulfonic acid in pumpkin (*Cucurbita maxima* L.) based on hydroponic culture: Uptake, translocation and biotransformation. *Environ. Pollut.* **252**, 804–812 (2019).
30. Rathinasabapathi, B. et al. Arsenic hyperaccumulation in the Chinese brake fern (*Pteris vittata*) deters grasshopper (*Schistocerca americana*) herbivory. *N. Phytol.* **175**, 363–369 (2007).
31. Basso, M. F. et al. Transcriptional responses of durum wheat to chronic chromium exposure reveal candidate proteins involved in metal detoxification and compartmentalization. *Environ. Exp. Bot.* **228**, 105953 (2024).
32. Marmiroli, M. et al. Copper oxide nanomaterial fate in plant tissue: nanoscale impacts on reproductive tissues. *Environ. Sci. Technol.* **55**, 10769–10783 (2021).
33. Li, Z. et al. Effects of coverly TF150® on the photosynthetic characteristics of grape. *Int. J. Mol. Sci.* **24**, 16659 (2023).
34. Yang, X. et al. Environmental evaluation of a distributed-centralized biomass pyrolysis system: a case study in Shandong. *China Sci. Total Environ.* **716**, 136915 (2020).
35. Rylott, E. L. & Bruce, N. C. Plants to mine metals and remediate land. *Science* **377**, 1380 (2022).
36. Qian, S. et al. Bioaccumulation of per- and polyfluoroalkyl substances (PFAS) in ferns: effect of PFAS molecular structure and plant root characteristics. *Environ. Sci. Technol.* **57**, 4443–4453 (2023).
37. Meng, J. et al. Tracing perfluoroalkyl substances (PFASs) in soils along the urbanizing coastal area of Bohai and Yellow Seas, China. *Environ. Pollut.* **238**, 404 (2018).
38. Li, F. et al. Quantitative characterization of short- and long-chain perfluorinated acids in solid matrices in Shanghai, China. *Sci. Total Environ.* **408**, 617–623 (2010).
39. Dou, X., Dai, H., Skuza, L. & Wei, S. Cadmium removal potential of hyperaccumulator *Solanum nigrum* L. under two planting modes in three years continuous phytoremediation. *Environ. Pollut.* **307**, 119493 (2022).
40. Xiang, Q. et al. Measuring log Kow coefficients of neutral species of perfluoroalkyl carboxylic acids using reversed-phase high-performance liquid chromatography. *Environ. Pollut.* **242**, 1283–1290 (2018).
41. Gu, Q., Wen, Y., Wu, H. & Cui, X. Uptake and translocation of both legacy and emerging per- and polyfluorinated alkyl substances in hydroponic vegetables. *Sci. Total Environ.* **862**, 160684 (2023).
42. Wang, S. et al. First report of a Chinese PFOS alternative overlooked for 30 years: its toxicity, persistence, and presence in the environment. *Environ. Sci. Technol.* **47**, 10163–10170 (2013).
43. Hong, J. et al. PFOS and its commercial alternative, 6:2 Cl-PFESA, induce multidrug resistance in pancreatic cancer. *Environ. Sci. Technol.* **58**, 22027–22038 (2024).
44. Pence, N. S. et al. The molecular physiology of heavy metal transport in the Zn/Cd hyperaccumulator *Thlaspi caerulescens*. *Proc. Natl. Acad. Sci. USA* **97**, 4956–4960 (2000).
45. Tian, S. et al. Cellular sequestration of cadmium in the hyperaccumulator plant species *Sedum alfredii*. *Plant Physiol.* **157**, 1914–1925 (2011).
46. Peng, J. et al. A pivotal role of cell wall in cadmium accumulation in the *Crassulaceae* hyperaccumulator *Sedum plumbizincicola*. *Mol. Plant.* **10**, 771–774 (2017).
47. Guo, X. et al. Root cell wall remodeling mediates copper oxide nanoparticles phytotoxicity on lettuce (*Lactuca sativa* L.). *Environ. Exp. Bot.* **200**, 104906 (2022).
48. Caffall, K. H. & Mohnen, D. The structure, function, and biosynthesis of plant cell wall pectic polysaccharides. *Carbohydr. Res.* **344**, 1879–1900 (2009).
49. Abbasi, S., Lamb, D. T., Choppala, G., Burton, E. D. & Megharaj, M. Antimony speciation, phytochelatin stimulation and toxicity in plants. *Environ. Pollut.* **305**, 119305 (2022).
50. Zhu, W. et al. Interactions between phenanthrene and polystyrene micro/nano plastics: Implications for rice (*Oryza sativa* L.) toxicity. *Environ. Pollut.* **337**, 122360 (2023).
51. Wu et al. The MYB transcription factor MYB103 acts upstream of *TRICHOME BIREFRINGENCE-LIKE27* in regulating aluminum sensitivity by modulating the O-acetylation level of cell wall xyloglucan in *Arabidopsis thaliana*. *Plant J.* **111**, 529–545 (2022).
52. Wang, J. et al. Abscisic acid alleviates mercury toxicity in wheat (*Triticum aestivum* L.) by promoting cell wall formation. *J. Hazard. Mater.* **449**, 130947 (2023).
53. Fu, Y. et al. Transcriptome and metabolome analysis reveal key genes and metabolic pathway responses in *Leersia hexandra* Swartz under Cr and Ni co-stress. *J. Hazard. Mater.* **473**, 134590 (2024).
54. Zhong, Y. & Chen, J. Ameliorative effects of Lanthanum(III) on Copper(II) stressed rice (*Oryza sativa*) and its molecular mechanism revealed by transcriptome profiling. *Plant Physiol. Biochem.* **152**, 184–193 (2020).
55. Becher et al. Cross-species microarray transcript profiling reveals high constitutive expression of metal homeostasis genes in shoots of the zinc hyperaccumulator *Arabidopsis halleri*. *Plant J.* **37**, 251–268 (2004).
56. Su, Y. H., McGrath, S. P., Zhu, Y. G. & Zhao, F. J. Highly efficient xylem transport of arsenite in the arsenic hyperaccumulator *Pteris vittata*. *N. Phytol.* **180**, 434–441 (2008).
57. Lu, L. et al. Enhanced root-to-shoot translocation of cadmium in the hyperaccumulating ecotype of *Sedum alfredii*. *J. Exp. Bot.* **59**, 3203–3213 (2008).
58. National Development and Reform Commission of China. Interim Measures for the Quality Management of Commercial Coal (NDRC Order No. 16) (2014). [https://www.gov.cn/zhengce/2021-06/25/content\\_5723620.htm](https://www.gov.cn/zhengce/2021-06/25/content_5723620.htm) (accessed July 18, 2025).
59. Grimison, C. et al. The efficacy of soil washing for the remediation of per- and poly-fluoroalkyl substances (PFASs) in the field. *J. Hazard. Mater.* **445**, 130441 (2023).
60. Shih, C. H. et al. Remediation of PFAS-impacted soils using magnetic activated carbon (MAC) and hydrothermal alkaline treatment (HALT). *Sci. Total Environ.* **912**, 168931 (2024).

61. Cheng, Y. et al. Electrothermal mineralization of per- and poly-fluoroalkyl substances for soil remediation. *Nat. Commun.* **15**, 6117 (2024).
62. Aghili, S. & Golzary, A. Greening the earth, healing the soil: a comprehensive life cycle assessment of phytoremediation for heavy metal contamination. *Environ. Technol. Innov.* **32**, 103241 (2023).
63. Espada, J. J. et al. Coupling phytoremediation of Pb-contaminated soil and biomass energy production: A comparative life cycle assessment. *Sci. Total Environ.* **840**, 156675 (2022).
64. Jin, Y. et al. Life cycle assessment to unravel environmental benefits and influencing factors of agricultural soil remediation strategies in China. *Resour. Conserv. Recy.* **211**, 107850 (2024).
65. Tavilla, G., Lanfranco, S. & Oenothera, L. a new genus of alien plant first reported in the Maltese Islands. *Phytotaxa* **705**, 203–211 (2025).
66. Mihulka, S. & Petr Pyšek, P. Invasion history of *Oenothera* congeners in Europe: a comparative study of spreading rates in the last 200 years. *J. Biogeogr.* **28**, 597–609 (2001).
67. Wang, J. & Aghajani, D. M. Techno-economic analysis of phytoremediation: a strategic rethinking. *Sci. Total Environ.* **902**, 165949 (2023).
68. Blumenkrantz, N. & Asboe-Hansen, G. New method for quantitative determination of uronic acids. *Anal. Biochem.* **54**, 484–489 (1973).
69. Dubois, M. et al. Colorimetric method for determination of sugars and related substances. *Anal. Chem.* **28**, 350–356 (1956).
70. Frisch, M. J. et al. Gaussian 16, Revision C.01; Gaussian, Inc.: Wallingford, CT, (2016). <https://gaussian.com/gaussian16/>.
71. Zhao, Y. & Truhlar, D. G. The M06 suite of density functionals for main group thermochemistry, thermochemical kinetics, non-covalent interactions, excited states, and transition elements: two new functionals and systematic testing of four M06-class functionals and 12 other functionals. *Theor. Chem. Acc.* **120**, 215–241 (2008).
72. Weigend, F. & Ahlrichs, R. Balanced basis sets of split valence, triple zeta valence and quadruple zeta valence quality for H to Rn: Design and assessment of accuracy. *Phys. Chem. Chem. Phys.* **7**, 3297–3305 (2005).
73. Marenich, A. V., Cramer, C. J. & Truhlar, D. G. Universal solvation model based on solute electron density and on a continuum model of the solvent defined by the bulk dielectric constant and atomic surface tensions. *J. Phys. Chem. B* **113**, 6378–6396 (2009).
74. Wang, M. et al. Molecular geometries and vibrational contributions to reaction thermochemistry are surprisingly insensitive to the choice of basis sets. *J. Chem. Theory Comput.* **19**, 5036–5046 (2023).
75. Chen, Z., Chen, J., Tan, S., Yang, Z. & Zhang, Y. Dechlorination helps defluorination: Insights into the defluorination mechanism of florfenicol by S-nZVI and DFT calculations on the reaction pathways. *Environ. Sci. Technol.* **58**, 2542–2553 (2024).
76. Love, M. I., Huber, W. & Anders, S. Moderated estimation of fold change and dispersion for RNA-seq data with DESeq2. *Genome Biol.* **15**, 550 (2014).

## Acknowledgements

The authors acknowledge the funding support from the “Pioneer” and “Leading Goose” R&D Program of Zhejiang Province (grant no. 2024C03233 to Y.Y.Z.), the National Natural Science Foundation of China (grant no. 42207431 to Y.Y.Z. and grant no. 42407001

to X.Y.G.), and the Research Center for Industries of the Future at Westlake University (grant no. WU2022C026 to Y.Y.Z.). The authors also thank the Instrumentation and Service Centers for Physical Sciences and Molecular Sciences and the High-Performance Computing Center at Westlake University for the assistance and use of their facilities.

## Author contributions

X.Y.G., L.W. and Y.Y.Z. conceived the idea and designed the experiments. X.Y.G. conducted the sample preparation, PFAS extraction, and most of the characterizations with the help of R.Y.W., X.X.Z., K.W. and Z.H.C.; X.Y.G. conducted the CIC, HPLC-MS/MS and GC-MS measurements with the assistance of X.X.Z. and J.C.; X.Y.G., W.Y.S., and J.C. assisted with the NMR tests; W.Y.S. and Y.Y.Z. conducted the DFT simulation; X.Y.G. and J.C. carried out the biomass pyrolysis and related analysis; X.Y.G. and L.W. performed the LCA analyses. X.Y.G., L.W. and Y.Y.Z. wrote and edited the manuscript. All aspects of the research were overseen by L.W. and Y.Y.Z. All authors discussed the results and commented on the manuscript.

## Competing interests

The authors declare no competing interests.

## Additional information

**Supplementary information** The online version contains supplementary material available at <https://doi.org/10.1038/s41467-025-65191-3>.

**Correspondence** and requests for materials should be addressed to Lei Wang or Yanyan Zhang.

**Peer review information** *Nature Communications* thanks Gianfranco Santovito, and the other, anonymous, reviewer(s) for their contribution to the peer review of this work. A peer review file is available.

**Reprints and permissions information** is available at <http://www.nature.com/reprints>

**Publisher’s note** Springer Nature remains neutral with regard to jurisdictional claims in published maps and institutional affiliations.

**Open Access** This article is licensed under a Creative Commons Attribution-NonCommercial-NoDerivatives 4.0 International License, which permits any non-commercial use, sharing, distribution and reproduction in any medium or format, as long as you give appropriate credit to the original author(s) and the source, provide a link to the Creative Commons licence, and indicate if you modified the licensed material. You do not have permission under this licence to share adapted material derived from this article or parts of it. The images or other third party material in this article are included in the article’s Creative Commons licence, unless indicated otherwise in a credit line to the material. If material is not included in the article’s Creative Commons licence and your intended use is not permitted by statutory regulation or exceeds the permitted use, you will need to obtain permission directly from the copyright holder. To view a copy of this licence, visit <http://creativecommons.org/licenses/by-nc-nd/4.0/>.

© The Author(s) 2025